Scientific Reports

https://doi.org/10.1038/s41598-026-44731-x

Article in Press

Mechanism of coal mass fracture expansion under drilling and pressure relief

Received: 9 October 2025

Accepted: 13 March 2026

Published online: 26 March 2026

Cite this article as: Liu K., Liu Y., Lu C. *et al.* Mechanism of coal mass fracture expansion under drilling and pressure relief. *Sci Rep* (2026). https://doi.org/10.1038/s41598-026-44731-x

Kun Liu, Yang Liu, Cai-Ping Lu, Lu-Hao Zhou, Qi-Xiang Zhou & Chao Wang

Mechanism of coal mass fracture expansion under drilling and pressure relief

Kun Liu [a], Yang Liu [a,1], Cai-Ping Lu [a], Lu-Hao Zhou [a], Qi-Xiang Zhou [b], Chao Wang [c]

[a] *Key Laboratory of Deep Coal Resource Mining (Ministry of Education), School of Mines, China University of Mining and Technology, Xuzhou, Jiangsu 221116, PR China*

[b] *Xiaoyun Coal Mine, Jining Energy Group, Jining, Shandong 272000, PR China*

[c] *Yankuang Energy Group Co., Ltd., Zoucheng 273500, China*

Abstract: To clarify the nonlinear transformation of coal from elastic energy storage to macroscopic fracture under borehole unloading, this study develops a multistage loading–unloading experimental system, incorporates acoustic emission monitoring, and utilises techniques such as moment tensor inversion, time-frequency analysis, and stress field inversion to examine the fracture propagation mechanisms and stress response characteristics of coal. The experimental findings indicate that borehole unloading causes local stress disturbances, which significantly influenced the fracture propagation paths and failure modes, thereby governing the macro-damage evolution process. The three-stage source mechanism analysis reveals that shear failure predominates throughout, while tensile failure notably increases during the secondary loading stage, indicating stage-dependent restructuring of stress distributions within the coal. Stress field inversion results reveal that in the initial loading stage, the maximum principal stress aligns southwest–northeast. During the secondary loading stage, the stress field shifts to a southeast–northwest inclined shear-dominated configuration, promoting shear-tension coupled fracturing. Borehole diameter affects fracturing behaviour: a 10-mm-diameter borehole initiates local high-energy events that inhibit crack propagation, whereas a 12-mm-diameter borehole enables energy cascade release and chain-like destruction. Time-frequency analysis shows that shear fractures mainly concentrate at 80–90 kHz with short-term energy aggregation; tensile fractures occur at 40–50 kHz, displaying mid-frequency expansion characteristics; and compression fractures are characterised by continuous low-frequency outputs at 10–20 kHz. Through theoretical analysis, a borehole pressure relief coal elastic-plastic damage model was developed to elucidate the control mechanisms of lateral pressure coefficient, borehole diameter, and stress level on the evolution of the plastic zone. This study enhances the understanding of crack propagation mechanisms in coal subjected to drilling-induced pressure relief in mines.

Keywords: Drilling pressure relief; Fracture propagation; Tensor inversion; Stress field inversion; Theoretical analysis; Time-frequency analysis

[1] Corresponding author. Tel.: +86 15152113681.
E-mail address: liuycumt@126.com (Y. Liu).

1 Introduction

As coal mining operations deepen and geological conditions become more complex, dynamic events such as rock bursts have emerged as primary hazards compromising mine safety [1–3]. Drilling and pressure relief can mitigate or eliminate rock burst hazards by adjusting stress distribution within the coal body, facilitating energy release, and altering the hazard potential of the coal body [4–6]. However, improper design of pressure relief drilling parameters may excessively weaken the strength of the coal body, adversely impacting the control of tunnel surrounding rock [7]. Rational design of pressure relief drilling parameters and effective management of coal body pressure relief strength are essential to balance the prevention of rock burst hazards with the control of tunnel surrounding rock deformation [8, 9].

Drilling and pressure relief induce stress redistribution within the coal/rock mass, simultaneously creating physical space for deformation. This deformation leads to the degradation of the coal/rock mass and the release of elastic energy [10–12]. This process entails the development and expansion of fractures caused by stress distribution discrepancies within the coal or rock mass, thereby diminishing its strength [13, 14]. The distribution and development of fractures are critical factors affecting the mechanical properties of the coal or rock mass [15–18]. Microscopic fracture characteristics within the coal or rock mass are essential for determining their macroscopic mechanical behaviour and significantly influence the deformation, failure, and strength properties of the coal or rock mass[19–23]. Under differing stress distributions, the types, scales, and propagation paths of fractures in the coal–rock mass vary considerably. Tensile fractures typically extend in the direction of maximum principal stress, whereas shear fractures often propagate along their initial orientation [24–27]. Additionally, fracture expansion and connectivity modify the surrounding stress field, leading to further deformation and failure of the coal or rock mass [28–30]. Thus, the expansion of fractures and the consequent weakening of strength in coal or rock masses under borehole de-coring pressure represent a progressive evolutionary process. Considering various factors that influence stress distribution within the rock mass—such as the existing stress environment, the physical and mechanical properties of the coal or rock mass, and drilling parameters—these elements collectively govern the fracture propagation characteristics of the coal or rock mass under drilling-induced pressure relief [31–34].

Accurate detection of internal fracture distribution within coal and rock bodies is fundamental to understanding their fracture propagation mechanisms. Advancements in fracture detection technologies have led to the extensive use of methods such as acoustic emission (AE), micro seismic (MS), electromagnetic radiation (EMR), computed tomography (CT), and nuclear magnetic resonance (NMR) for investigating deformation and fracture mechanisms in coal and rock

specimens [35–39]. Among these, AE (laboratory scale) and MS (macro-engineering scale) are non-destructive testing techniques [40,41] that continuously monitor fractures. Their mature analytical techniques make them the most widely applied methods for monitoring and analysing coal and rock fractures today. AE continuously records the macroscale three-dimensional characteristics of fracture development and propagation in coal and rock. For instance, AE event localisation reflects the temporal evolution of spatial fracture distribution, AE impact counts quantify the number of fracture events, and AE energy/amplitude characterize the scale of fracture development [42–44]. Additionally, calculating the AE b-value enables the identification of precursors to coal and rock failure[45,46]. Analysing AE signals in the frequency domain and RA values allows for the characterisation of crack propagation modes in coal and rock [47,48]. Furthermore, utilising AE waveform signals for coal and rock wave velocity tomography and fracture source moment tensor inversion facilitates precise characterisation of stress field evolution and fracture patterns, thereby providing more accurate analytical methods and techniques to elucidate the theoretical mechanisms underlying coal and rock deformation and failure [49–53].

During unloading, coal rock drilling becomes a drilling excavation process subjected to external loads, with fracture propagation driven by both these external stresses and excavation-induced unloading. The initiation and growth of fractures within the coal body during borehole de-stressing represent a continuous evolutionary process. Unlike stress-induced fracturing, excavation-induced fracture expansion occurs more rapidly and on a smaller scale, which complicates the analysis of fracture evolution.

This study employs multistage loading–unloading experiments combined with real-time AE monitoring to investigate the multiparameter evolution characteristics of acoustic emissions in coal bodies during various stages of borehole unloading. AE signal tensor inversion is utilised to examine fracture propagation patterns and the characteristics of coal bodies under borehole unloading, as well as to interpret the stress field distribution at different stages. The macro- and micro-fracture mechanisms of coal bodies under borehole unloading are thus elucidated.

2 Experimental design and methods

2.1 Materials and Sample Preparation

The experimental samples consisted of coal specimens obtained from in-situ coal cores of the No. 3 coal seam in the Shandong mining area of China. The coal samples were prepared into two sets: cylindrical specimens measuring Φ50 mm × 100 mm (diameter × height) and cubic specimens sized 50 mm × 50 mm × 100 mm (length × width × height). To ensure seamless contact between the sample surfaces and the sensor, optimise ultrasonic wave propagation, minimise scattering and

attenuation, and enhance interface coupling efficiency and signal detection sensitivity, the surfaces were meticulously ground smooth using fine sandpaper in accordance with standard procedures, maintaining an average dimensional error within 0.5 mm. Furthermore, a thin layer of high-vacuum silicone grease was uniformly applied as an acoustic couplant between the acoustic emission sensors and the polished coal surfaces. This effectively eliminated interfacial air gaps, further guaranteeing the high-fidelity transmission of high-frequency signals. This method effectively prevented errors from dimensional variances and improved the reliability and comparability of the test results. After preparation, ultrasonic re-screening was performed to eliminate discrete anomalies and ensure homogeneity.

2.2 Experimental apparatus and experimental plan

The experimental system comprises an ultrasonic testing system, a stress loading system, a drilling and pressure relief system, and an acoustic emission (AE) monitoring system, as illustrated in Figure 1.

During ultrasonic testing, the OLYMPUS V103-RM probe, with a diameter of 12.7 mm and a sampling frequency of 1 MHz, was employed for contact ultrasonic measurements of coal samples, enabling accurate wave velocity data acquisition at high frequencies. Wave velocity was determined based on the measured thickness of the coal sample and the propagation time of the ultrasonic wave from emission to reception, resulting in a value of 2500 m/s.

Single-axis loading was performed using an MTS C64.106 testing machine with a 1000 kN capacity. This machine offers three control modes: force, displacement, and strain; it supports data acquisition at 1000 Hz and provides a displacement resolution of 0.2 μm.

The drilling and pressure relief device features a proprietary rail-guided structure, incorporating high-rigidity linear guides with bidirectional positioning accuracy of ±0.02 mm and tungsten carbide twist drills (Φ8/10/12 mm) with a top angle of 118°. Drilling positioning and feed adjustments are managed through a mechanical transmission system. The device supports both manual and semi-automatic operations, accommodating various hole diameters with a processing error of $\leqslant$ 0.5 mm. The Φ12 mm drill bit achieves optimal chip evacuation efficiency through a main cutting angle of 55° and a secondary cutting angle of 25°; it is equipped with a mechanical ratchet that offers three-speed adjustments (1.5/2.5/3.5 mm/s) to handle the heterogeneous hardness of coal layers. During drilling, chips are removed manually, and a dual-guide block anti-deflection mechanism ensures the straightness of the hole.

The AE signals are captured by the PIC-2 system, which includes 8-channel G150-1 sensors (70–280 kHz, dynamic range > 68 dB) and 2/4/6 preamplifiers featuring 40 dB gain and 1 kHz–1 MHz bandpass filters to minimise noise.

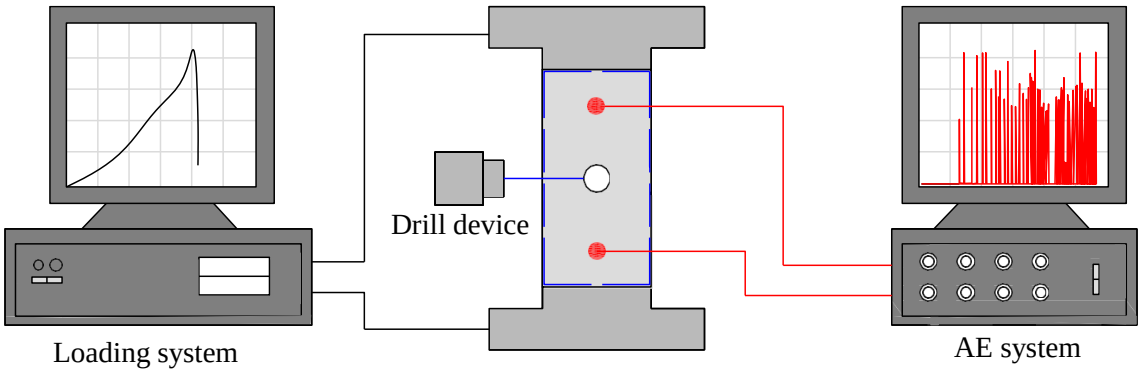

Figure 1 Schematic diagram of the test system

To determine the initial stress condition for the loading–unloading tests, cylindrical coal specimens (Φ50 mm × 100 mm) cored from the No. 3 coal seam in the Shandong mining area were subjected to uniaxial compression. Total of three specimens were tested, obtaining an average unaxial compressive strength (UCS) of 12.97 MPa. This value was used solely to define the initial loading level of the cubic specimens. All drilling and unloading experiments in this study employed cubic coal specimens with the size of 50 mm × 50 mm × 100 mm (length × width × height). This specimen size was selected to comply with international standards for specimen dimensions. Furthermore, compared to cylindrical specimens, rectangular specimens facilitate drilling operations and more effectively simulate stress redistribution around the drill hole and crack propagation processes under initial loading conditions. A multistage loading-unloading experiment was designed to explore the underlying mechanisms of this phenomenon. Axial displacement-controlled loading was applied at a rate of 0.3 mm/min to determine the unconfined compressive strength of the specimens (UCS = 12.97 MPa), establishing the initial stress at 55% of UCS (7.2 MPa). The experimental procedure consisted of four phases: initial loading, drilling and unloading, static loading, and secondary loading. In the initial loading phase, the axial load was set to 55% UCS (7.2 MPa). A dual closed-loop force–displacement control system was utilised to eliminate end friction effects during loading.

During the drilling and unloading phase, vertical axial drilling was performed using a drill rig with a feed rate of 2.5 mm/s, a hole diameter of 12 mm, and a drilling depth of 50 mm to penetrate the axis of the specimen. In the static loading phase, an axial load of 7.2 MPa was maintained for 480 seconds to reduce local stress concentrations and eliminate creep effects. In the secondary loading phase, axial displacement was applied at a rate of 0.5 mm/min until macro-scale specimen failure occurred, while a multichannel AE monitoring system simultaneously collected full-waveform signals.

To investigate the crack propagation responses of specimens with varying drilling parameters under a constant initial stress field, two control experiments were conducted with borehole

diameters of 8 mm and 10 mm, respectively. Borehole diameter parameters were established using the critical fracture zone radius theory to ensure that the stress gradient from the unloading volume, generated by various borehole diameters, fell within the damage threshold range of the coal body.

2.3 Methods

(1) AE localisation

Accurate determination of the P-wave first arrival time is crucial for source localisation and subsequent mechanical inversion. This study utilises the Akaike Information Criterion (AIC) [54], defined mathematically as follows:

$$AIC(k) = k \cdot log(var(x[1,k])) + (N-k) \cdot log(var(x[k+1,N])), \quad (1)$$

In this equation, k represents the segmentation point, and N denotes the time window length. The optimal P-wave arrival time is determined by minimising the AIC value. To improve the signal-to-noise ratio, the original signal is preamplified with a 40 dB gain and then processed through a bandpass filter with a bandwidth of 1 kHz to 1 MHz to remove environmental noise interference. For events with signal-to-noise ratios below 5 dB, manual verification is performed by assessing waveform polarity, amplitude envelope shape, and consistency with adjacent sensors to ensure positioning errors are $\leqslant$1 mm.

The acoustic emission localisation method leverages the propagation characteristics of AE signals within the medium. This localisation technique utilises a sensor array to gather signals and determine the spatial coordinates of the AE source by applying a nonlinear least-squares method based on the time difference of arrival (TDOA) [55]. The localisation is governed by the following equation:

$$\sqrt{(x-x_i)^2+(y-y_i)^2+(z-z_i)^2} - \sqrt{(x-x_1)^2+(y-y_1)^2+(z-z_1)^2} = v(t_i - t_1)(i = 2, \ldots, n), \quad (2)$$

where (x, y, z) denote the coordinates of the AE event source, while (x_i, y_i, z_i) correspond to the coordinates of the i-th sensor. The variable v represents the wave velocity, t_0 is the absolute initiation time of the event, and t_i denotes the reception time of the signal at the i-th sensor.

By leveraging the time differences in AE signal arrivals from eight sensors, a nonlinear system of equations is established. Assuming constant wave velocity propagation within the coal body, the source coordinates are determined using an optimisation algorithm. The optimisation objective is defined by the equation:

$$\min_{x,y,z} \sum_{i=2}^{n} [\Delta d_i^{calc} - v\Delta t_i^{obs}]^2, \quad (3)$$

where Δd_i^{calc} denotes the distance difference and Δt_i^{obs} indicates the time difference.

(2) Moment tensor inversion

The moment tensor inversion method presented in this paper employs the Absolute Moment Tensor Inversion (AMTI) model, which constructs the displacement field equation using the Green's function for a uniformly isotropic medium [56]:

$$u_n(t) = G_{npq}(t) * M_{pq}, \quad (4)$$

where $u_n(t)$ represents the displacement field recorded by the nth sensor; M_{pq} denotes the component of the symmetric tensor (p, q = 1, 2, 3); $G_{npq}(t)$ represents the Green's function of a uniform isotropic medium, expressed analytically as

$$G_{npq}(r,t) = \frac{1}{4\pi\rho v_p^3}(\delta_{pq} - 2\gamma_n\gamma_q)\frac{1}{r}\delta(t - \frac{r}{v_p}) \ , \quad (5)$$

where ρ signifies the coal body density; v_p represents the elastic wave velocity; γ_n denotes the cosine of the sensor direction; r indicates the source distance; and δ_{pq} represents the Kronecker delta function. After discretising the displacement field equation, a system of linear equations is established:

$$u=GM, \quad (6)$$

In this equation, u represents the initial amplitude of the waveform recorded by the sensor and is an n-dimensional vector. G comprises the Green's functions in the sensor coordinate system, forming an $n \times 6$ matrix. The mode tensor vector is defined as $\boldsymbol{m} = [M_{11}, M_{22}, M_{33}, M_{12}, M_{13}, M_{23}]^T$.

Following the classification method proposed by Feignier & Young [57], the relative contributions of volume change and shear deformation in the source mechanism are quantified using the following formula:

$$R = \frac{tr(M_{ij})\times 100}{|tr(M_{ij})| + \Sigma|M_i^*|}, \quad (7)$$

where $tr(M_{ij})$ denotes the trace of the moment tensor, indicating the intensity of volume change (positive values signify expansion, while negative values indicate contraction). $|tr(M_{ij})| + \Sigma|M_i^*|$ represents the sum of the absolute values of the principal moments (eigenvalues) of the moment tensor, reflecting the total shear deformation intensity. The denominator normalises the combined contributions of volume change and shear deformation to ensure the proportionality of the R value.

Based on the R value range, seismic source mechanisms are categorised into three types: tensional events (volume expansion dominant) with $R > 30$; shear events (shear deformation dominant) with $30 \leqslant R \leqslant 30$; and implosion events (volume contraction dominant) with $R < -30$.

(3) Spectrum analysis

This study generates time–frequency maps using the Stockwell transform, which enables time–frequency localisation analysis of non-stationary signals through a frequency-adaptive Gaussian

window function. The core formula [58] is as follows:

$$S(\tau, f) = \int_{-\infty}^{\infty} x(t) \cdot \frac{|f|}{\sqrt{2\pi}} e^{-\frac{f^2(\tau-t)^2}{2}} e^{-i2\pi f t} dt, \quad (8)$$

In this equation, $x(t)$ denotes the input signal; τ denotes the time centre point; and f represents the analysis frequency.

The width of the Gaussian window is adaptively adjusted based on frequency, and its discrete form S is transformed as follows:

$$S[m, n] = \sum_{k=0}^{N-1} x[k] \cdot \frac{f_n}{\sqrt{2\pi}} e^{-\frac{f_n^2(m\Delta t - k\Delta t)^2}{2}} e^{-i2\pi f_n k\Delta t}, \quad (9)$$

In this equation, $x[k]$ denotes the discretely sampled signal, $m\Delta t$ represents the time centre, f_n indicates the analysis frequency, Δt indicates the sampling interval, and N stands for the signal length.

(4) Stress field inversion

Stress field inversion is based on linear elasticity theory, assuming that the slip direction on the fault plane aligns with the local shear stress direction. By applying least-squares fitting to extensive seismic source mechanism data, the principal stress directions and stress shape factor R values of the stress tensor are determined.

$$R = \frac{\sigma_2 - \sigma_3}{\sigma_1 - \sigma_3}, \quad (10)$$

This study is based on joint iterative inversion theory [59]. Adhering to the principle of minimal slip deviation, the theoretical slip direction is compared with the predicted slip direction influenced by the stress tensor, identifying the fault plane with the least slip deviation as the true fault plane. The three-dimensional stress field is inverted using statistical analysis of the source mechanism parameters, and the principal stress directions are determined through feature decomposition:

$$\tau v_i = \lambda_i v_i (i = 1,2,3), \quad (11)$$

where λ_i represents the eigenvalues and v_i the corresponding eigenvectors.

The discrepancy between observed and theoretical sliding directions is minimized, subject to the friction coefficient $\mu \in [\mu_{min}, \mu_{max}]$:

$$\min_{\tau} \sum_{k=1}^{N} \| s_k - \frac{\tau n_k}{\|\tau n_k\|} \|^2 \, s.t. \mu \in [\mu_{min}, \mu_{max}], \quad (12)$$

where s_k denotes the observed sliding direction vector of the k-th event, and n_k represents the fault normal vector.

By dynamically adjusting noise tolerance and iteration counts in stages, high-precision reconstruction of stress fields across multiple loading phases is achieved, producing primary source mechanisms, including the optimal stress tensor, principal stress directions, shape ratio, true fault geometry, primary focal mechanism, optimal friction coefficient, and error assessment.

3 Macro-destruction characteristics of coal body after drilling and pressure relief

To investigate the mechanical response and fracture evolution mechanisms of coal under borehole unloading conditions, borehole disturbance was introduced during uniaxial loading. AE technology was employed to obtain stress–strain characteristics, AE event responses, and dynamic changes in energy parameters throughout the loading process. In total, 892 valid AE events were recorded. By integrating standard stage division, AE event temporal progression, and three-dimensional spatial visualisation analysis, this study systematically elucidates the nonlinear failure behaviour and crack propagation characteristics of coal under the combined influences of pressure relief disturbance and loading.

3.1 Evolutionary characteristics of stress and fracture event numbers in coal bodies during drilling and pressure relief

Figure 2 depicts the stress-strain relationship, AE event temporal evolution, and energy response trend during the borehole unloading test. Employing stress loading methods and AE event characteristics, the experimental process is divided into four stages: initial loading, borehole unloading, static loading, and secondary loading.

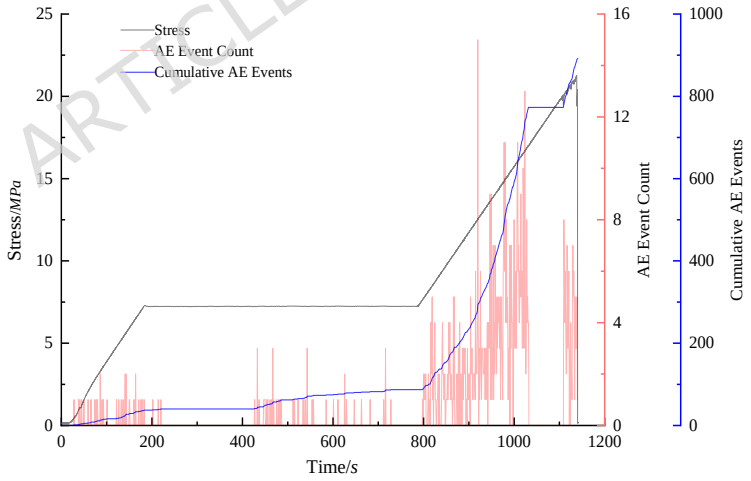

(a) Stress-event number time series correlation

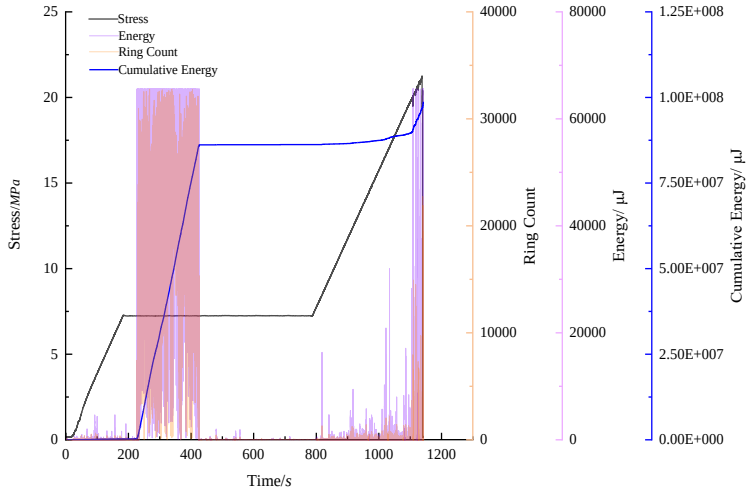

(b) Energy-ring count coupling response

Figure 2 Basic mechanical parameters of the coal body under drilling and pressure relief

In the initial loading stage (0–225 s), stress linearly increased from 0 MPa to 7.2 MPa, strain increased from 0.038 to 0.056, and the elastic modulus was approximately 0.4 GPa, indicating typical linear elastic deformation behaviour. Forty AE events were recorded, with a low event rate, suggesting that this phase primarily involved primary fracture closure and elastic energy storage, with limited microfracture nucleation. The fracture mechanism remained in an early disturbance phase. Upon entering the borehole decompression stage (226–426 s), stress stabilised at 7.2 MPa, and strain showed no significant rebound, indicating that the borehole process did not induce macrostructural damage. Because of considerable environmental noise, only one low-energy AE event was detected during this stage, originating near the borehole wall. This suggests that the pressure relief operation caused only localised stress disturbances without initiating extensive fracture propagation. The coal body maintained relatively intact structural integrity. During the static loading phase (427–784 s), stress remained constant while AE events increased to 45, indicating heightened local stress concentrations and the redistribution of internal fractures within the coal body alongside subcritical crack propagation. Although AE activity rose compared to the preceding phase, the overall process remained low-energy, characterised by gradual damage accumulation primarily through the expansion of microfractures along existing structural planes. As the sample transitioned into the secondary loading stage (785–1140 s), stress sharply increased from 7.2 MPa to 21.26 MPa, and strain rose to 0.066. During this stage, AE events surged to 806, accounting for over 90% of total events. Notably, around 920 s, the number of events markedly increased, with the AE event growth rate significantly elevated and the cumulative event curve slope rising to 15.1 events/s^2, indicating entry into a nonlinear damage acceleration stage. In this phase, crack co-evolution became evident, with microfracture activities concentrated along the primary fracture plane. The stress–time curve and surge in event numbers showed high synchrony, reflecting the

strong coupling between strain energy accumulation and fracture activity. At approximately 1120 s, event numbers peaked, indicating that the coal body had entered the precursor stage of macroscopic instability.

In summary, the drilling and pressure relief procedure did not inflict extensive damage on the coal body but significantly modified its local stress field and microstructure. During subsequent secondary loading, it accelerated crack aggregation and energy release, causing a transition in the failure mode from discrete cracking to through-fracturing. The samples exhibited typical nonlinear evolution, marked by gradual damage progression followed by sudden instability.

3.2 AE Spatiotemporal Distribution and Energy Evolution Analysis

The spatiotemporal dynamics of AE events reflect the intricate migration and microstructural changes during the fracturing process of the sample. To illustrate the spatiotemporal characteristics and energy distribution of AE events in the drilled coal body during pressure relief, a four-stage spatiotemporal evolution sub-diagram is constructed (Figure 3), revealing the multidimensional dynamic laws governing damage evolution.

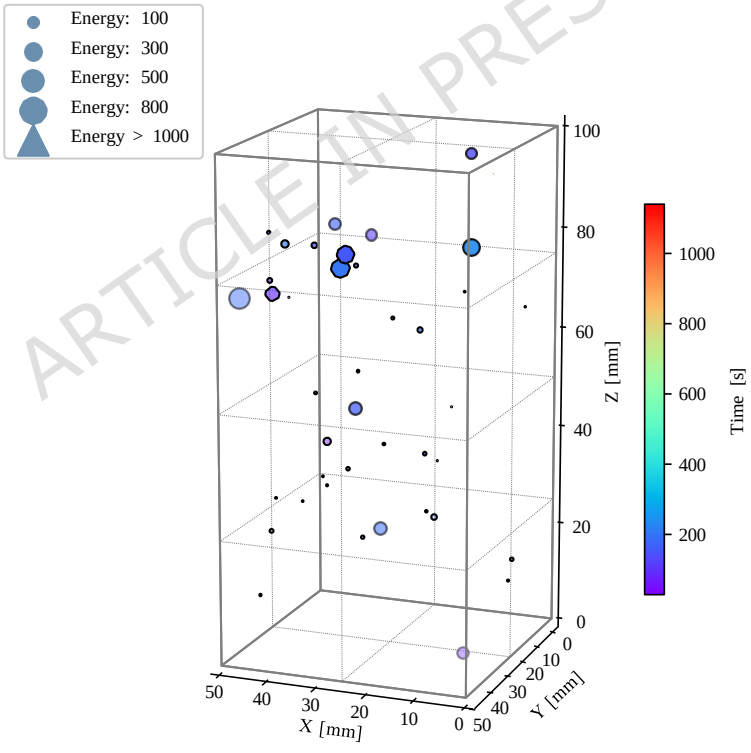

(a) Initial loading phase

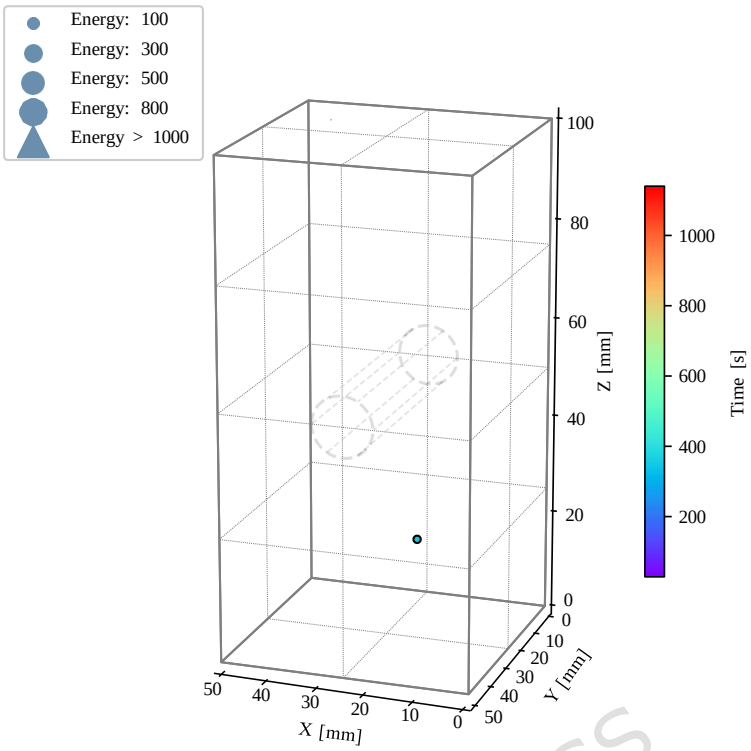

(b) Drilling and pressure relief stage

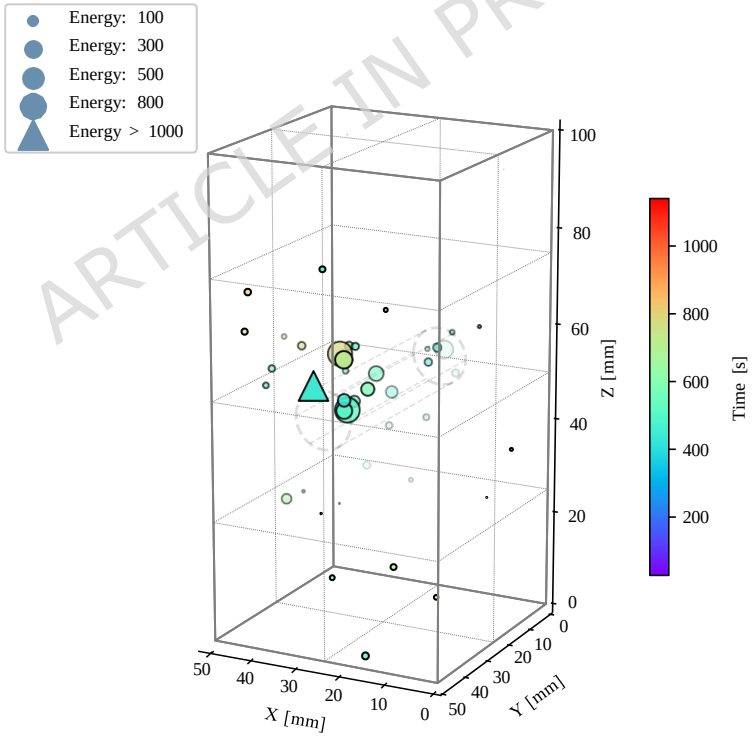

(c) Constant load stage

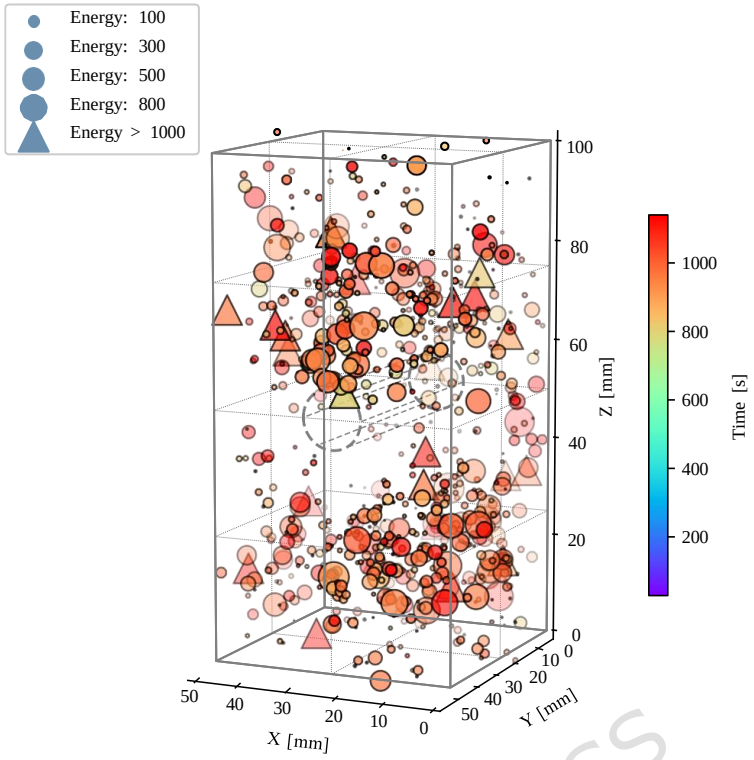

(d) Secondary loading phase

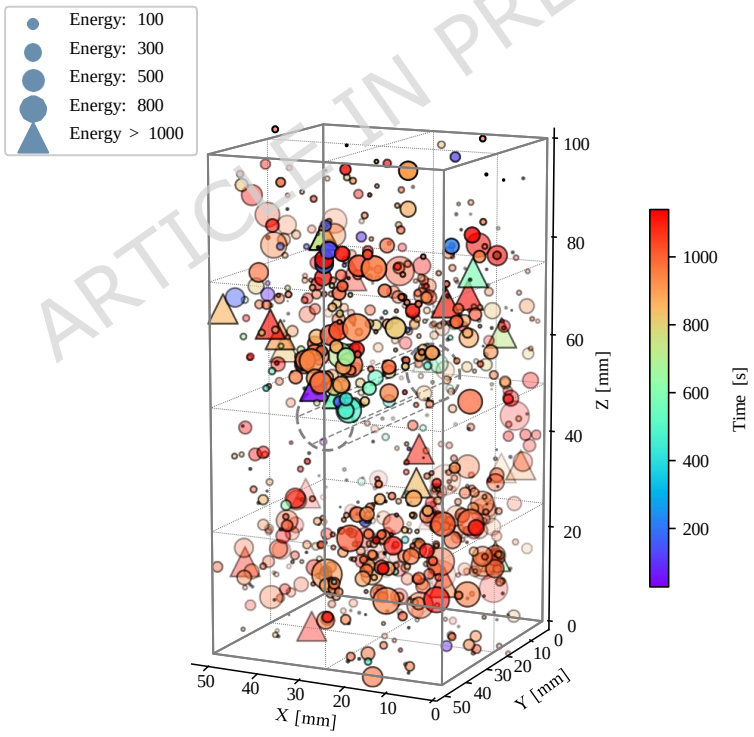

(e) Entire process

Figure 3 Spatial and temporal evolution distribution of AE events in the coal body during drilling and pressure relief

Initially, AE event sources were broadly distributed with low energy levels, primarily showing low-frequency and low-amplitude responses, and a ringing count rate below 500 counts/s. Events

were randomly scattered throughout the specimen, indicating the closure of primary fractures and the dispersed initiation of microcracks. AE activity remained stable during this stage, with no dominant fracture mode emerging. During the borehole unloading stage, event responses nearly ceased, with only a single low-energy event (approximately 47 μJ) occurring near the borehole edge. This signifies a period of minimal fracture activity intensity. Unloading operations minimally disrupted the macrostructure but induced localised stress field restructuring, thereby weakly triggering subsequent crack propagation. In the static loading stage, the few AE events observed gradually originated near the centre of the specimen, with energy levels slightly higher than the previous stage. These events exhibited a striped distribution aligned with the maximum principal stress direction, indicating that crack propagation was driven by stress redistribution during this phase. This process gradually established the basic shape of the main fracture path, with energy release mainly characterised by minor secondary increases. In the secondary loading stage, as the external load rapidly intensified, both the number and energy of AE events increased exponentially. High-energy events (500–700 μJ) appeared in large numbers, accompanied by multiple high-frequency ringing pulses (>5000 counts/s). Event sources concentrated on both sides of the drill hole and within the main fracture zone, aggregating in a striped pattern along the inclination direction, thereby creating a distinct directional distribution. The energy density peaked at 920 s, indicating that fractures began to develop synergistically and ultimately formed a continuous structure. During this stage, AE responses significantly intensified, energy release became concentrated, ringing pulses grew denser, and fracture rupture behaviour became increasingly violent, marking the coal's transition into the main controlled stage of unstable rupture.

Overall, the spatiotemporal distribution and energy parameters of AE events exhibit an evolutionary progression from being discrete and disordered to becoming concentrated and interconnected across various phases. In the initial phase, the primary processes involved disruptions of the original structure and elastic responses. During the intermediate phase, crack migration and redistribution increasingly manifested. In the final phase, strain energy drove the rapid formation of the main fracture surface and the focused release of energy. Although borehole disturbances did not immediately trigger macroscopic failure, they were pivotal in promoting the subsequent structural evolution of the coal body, acting as a potential catalyst for converting local instability into comprehensive fracturing.

4 Microfracture mechanism of coal mass during drilling and pressure relief

4.1 AE event source mechanism characteristics

To investigate the evolutionary characteristics of fracture mechanisms in the coal body under borehole unloading conditions, an absolute moment tensor inversion method was employed, utilising P-wave initial arrival amplitude picking to perform source mechanism analysis on 24 representative AE events selected from 892 valid events across three stages: initial loading, static constant loading, and secondary loading. To ensure the reliability and accuracy of the inversion results, these 24 representative events were strictly filtered based on the following specific criteria: (1) high signal-to-noise ratio with unambiguous P-wave first arrivals to minimize initial amplitude picking errors; (2) simultaneous activation of at least six sensors to provide sufficient independent equations for mathematically constraining the moment tensor matrix; and (3) uniform spatial distribution and extensive temporal coverage strategically sampled across the three distinct loading stages. The fault plane solutions and fracture types for the events are detailed in Tables 1 and 2, and the spatial distribution of the AE event source mechanisms is illustrated in Figure 4.

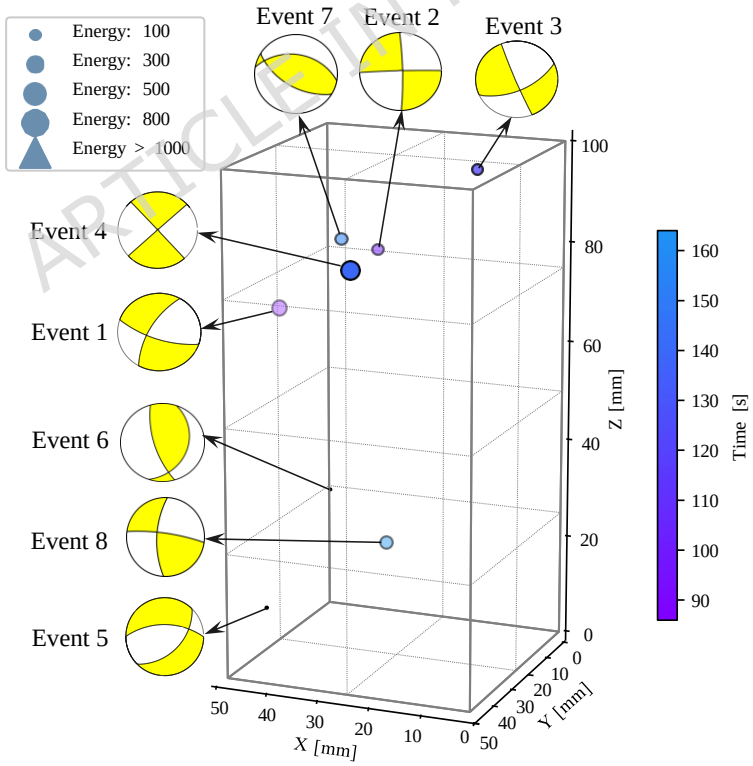

(a) AE event distribution during the initial loading phase

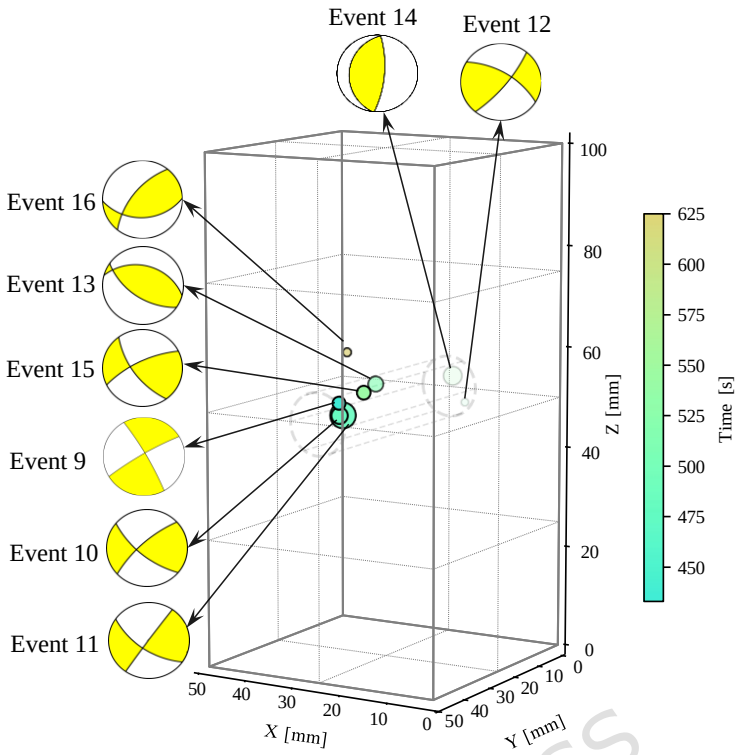

(b) Distribution of AE events during the static loading phase

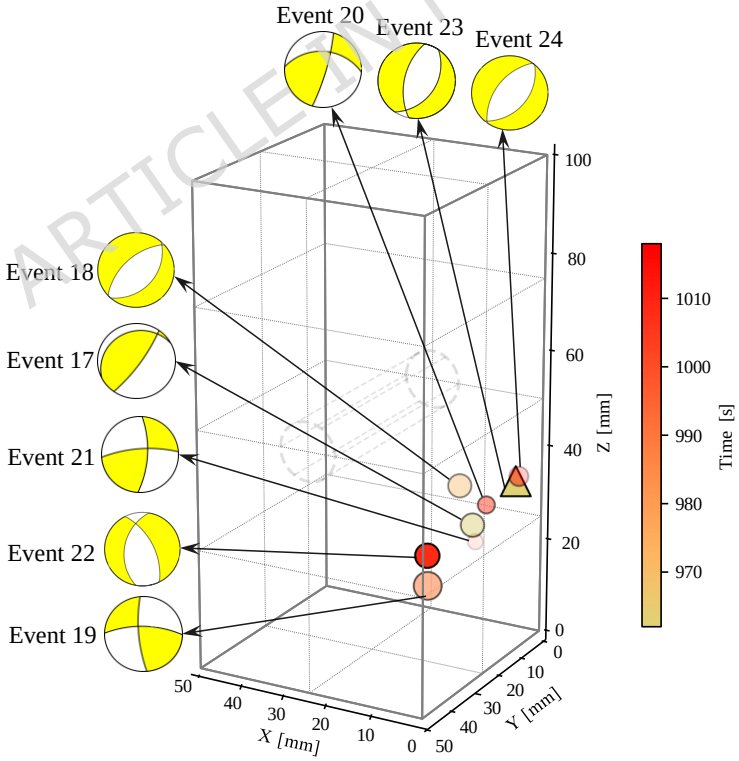

(c) Distribution of AE events in the secondary loading phase

Figure 4 Distribution of AE events in the coal body during drilling and pressure relief and source mechanism

Table 1 Full tensor, ratio, and fracture type of AE events in coal bodies during borehole decompression

Events	FMT	R value	Standard Error	Type of rupture
#1		9.01	0.19E+00	shear failure
#2		−20.30	3.38E-02	shear failure
#3		−15.31	8.75E-02	shear failure
#4		3.50	9.17E-02	shear failure
#5		51.36	0.15E+00	tensile failure
#6		−16.24	5.84E-03	shear failure
#7		−52.47	0.13E+00	compression-dominated failure mode
#8		−8.02	7.68E-02	shear failure
#9		37.9	7.08E-02	tensile failure
#10		−1.26	1.07E-02	shear failure
#11		7.54	9.81E-02	shear failure
#12		−15.66	0.12E+00	shear failure
#13		−27.77	0.23E+00	shear failure
#14		−37.53	5.86E-02	compression-dominated failure mode
#15		−19.16	4.15E-02	shear failure
#16		−8.67	4.44E-02	shear failure
#17		−12.46	0.47E+00	shear failure
#18		36.41	0.19E+00	tensile failure
#19		−34.66	0.22E+00	compression-dominated failure mode
#20		9.50	0.46E+00	shear failure
#21		−32.30	0.59E+00	compression-dominated failure mode

#22		38.82	0.20E+00	tensile failure
#23		38.20	0.31E+00	tensile failure
#24		38.00	0.14E+00	tensile failure

Table 2: Interpretation of AE events in the coal body during drilling and unloading, and fault plane analysis and fault types

Events	DC	Primary fault plane			Auxiliary fault plane			Type of fault plane
		Strike [°]	Dip [°]	Rake [°]	Strike [°]	Dip [°]	Rake [°]	
#1		209.8	63.5	-155.9	108.5	68.6	-28.7	Right-lateral oblique fault
#2		358.8	84.1	-177.6	268.6	87.6	-5.9	right-lateral strike-slip fault
#3		65.4	57.3	-4.7	158.0	86.0	-147.2	left-lateral strike-slip fault
#4		317.6	89.5	0.5	227.6	89.5	179.5	left-lateral strike-slip fault
#5		44.9	44.3	-126.0	270.3	55.6	-60.1	Right-lateral oblique fault
#6		19.3	27.0	122.9	163.3	67.6	74.5	right-lateral reverse fault
#7		280.0	37.5	73.0	121.1	54.4	102.6	reverse fault
#8		182.8	64.9	167.9	277.9	79.1	25.6	right-lateral strike-slip fault
#9		239.4	82.6	172.7	330.3	82.8	7.5	right-lateral strike-slip fault
#10		129.8	66.8	161.1	227.5	72.7	24.4	right-lateral strike-slip fault

#11		124.5	61.5	178.3	215.3	88.5	28.5	right-lateral strike-slip fault
#12		301.3	61.8	163.5	39.2	75.5	29.2	right-lateral strike-slip fault
#13		285.0	36.0	74.1	124.4	55.6	101.2	reverse fault
#14		187.7	20.2	93.1	4.3	69.9	88.8	reverse fault
#15		143.5	63.4	157.6	243.9	70.1	28.5	right-lateral reverse fault
#16		87.8	39.9	131.4	218.8	61.2	61.0	right-lateral reverse fault
#17		242.5	13.6	116.4	35.5	77.9	83.9	right-lateral reverse fault
#18		41.4	36.3	-94.6	227.0	53.8	-86.7	normal fault
#19		271.2	66.9	15.4	175.0	75.8	156.1	left-lateral strike-slip fault
#20		274.0	38.9	164.8	15.9	80.5	52.1	right-lateral strike-slip fault
#21		3.1	67.9	18.7	265.8	72.7	156.7	left-lateral strike-slip fault
#22		190.1	39.3	-59.7	333.1	56.9	-112.4	left-lateral oblique normal fault
#23		34.1	37.3	-72.1	192.0	54.8	-103.1	normal fault
#24		40.4	40.2	-87.1	216.7	49.8	-92.4	normal fault

The results indicate that the three-stage event rupture mechanism can be classified into three categories: shear rupture ($-30 \leqslant R \leqslant 30$), tensile rupture ($R > 30$), and compressional rupture ($R < -30$). Each mechanism aligns with specific fault geometric parameters and activity characteristics. Shear rupture is predominant across all stages, with fault types mainly consisting of strike-slip and oblique reverse faults, indicative of a slip rupture process driven by local stress

adjustments. Tensile rupture events primarily occur during the secondary loading stage, featuring fault types such as normal and oblique normal faults. The slip angles typically deviate from pure shear angles, highlighting rupture characteristics dominated by tensile stress. Compressional rupture events are less common, are mainly found in regions of high stress concentration, and are characterised by reverse and strike-slip reverse faults, reflecting slip ruptures caused by shear-compressional interactions.

The statistical distribution of fracture types across different stages further clarifies the stress response mechanisms governing coal body fracture evolution. In the initial loading stage, shear fractures are dominant, with minimal tensile and compressive fractures. During the static loading stage, shear fracture intensifies, fault types become more complex, and composite characteristics involving multiple mechanisms emerge. In the secondary loading stage, the proportion of tensile fractures rises significantly while shear fractures diminish, indicating that tensile stress predominates within the coal body following unloading. To further validate the effectiveness of seismic source mechanism identification, Figure 5 illustrates the distribution characteristics of AE events in the T–K diagram. The scatter plot in Figure 5a reveals that most events cluster near the DC region, indicating that shear fracturing predominates during the borehole unloading process. Additionally, some fracturing events exhibit a dispersed distribution, suggesting that tensile or compressive forces govern fracturing patterns in localised areas. The density distribution map (Figure 5b) shows that the majority of events concentrate within the primary shear fracture control zone, displaying high-density aggregation. In contrast, non-shear-dominated tensional and compressive fracture events are more scattered, highlighting spatial evolution differences and stage-specific characteristics of various fracture mechanisms.

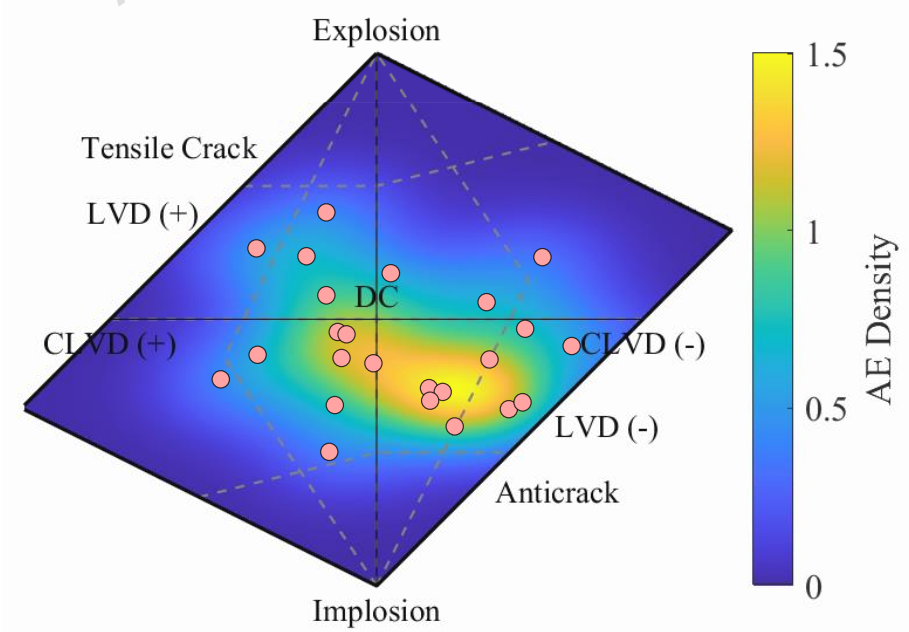

Figure 5 T-K diagram of borehole pressure relief coal body source distribution

4.2 Local stress field inversion and stress disturbance characteristics

To elucidate the evolution of local stress states in coal bodies at different loading stages, this study employs a three-dimensional principal stress field inversion method based on source mechanisms derived from moment tensor inversion, utilising a parameter dynamic self-adaptive optimisation approach. During the initial loading stage, accounting for the signal fluctuations during the elastic deformation period, the noise standard deviation was set to 4.0°, with 150 iterations, and the shape ratio range adjusted to 0.1–1.0. Monte Carlo simulations generated 150 noise samples to accommodate the non-steady-state characteristics of the initial signals. During the static constant load stage, reduced environmental noise allowed the noise level to decrease to 2.5°, the iteration count lowered to 80. In the secondary loading stage, to prevent signal contamination from damage accumulation, noise tolerance was increased to 5.5°, the iteration count rose to 300, and the shape ratio range was expanded to 0.5–1.0, covering the extreme stress zone. The dynamic convergence criteria were confirmed through Bootstrap resampling to ensure the robustness of the inversion results. The inversion outcomes are shown in Figure 6, with principal stress axis parameters detailed in Tables 3–5.

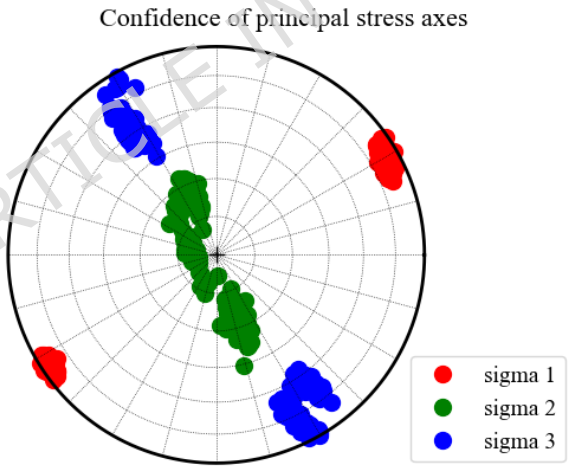

(a) Stress field direction during the initial loading stage (confidence level 95%)

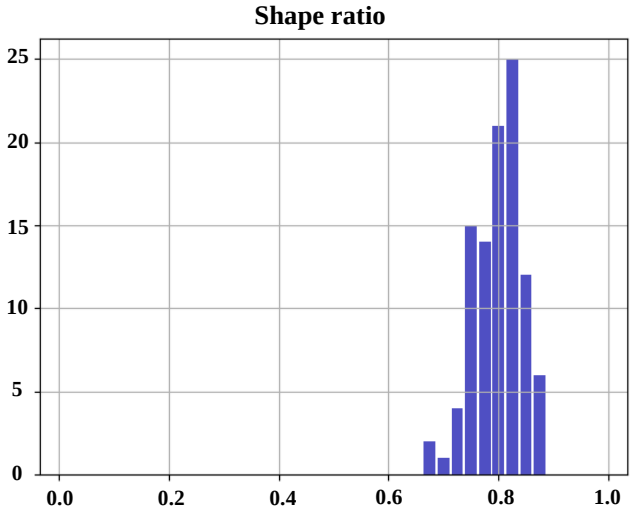

(b) Frequency distribution of stress shape factor R in the initial loading stage

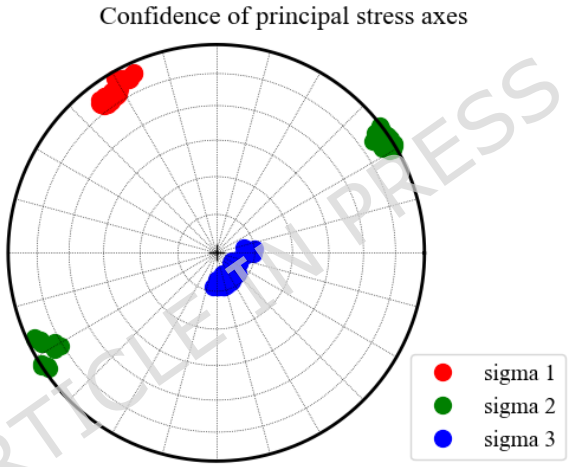

(c) Stress field direction during the static loading stage (confidence level 95%)

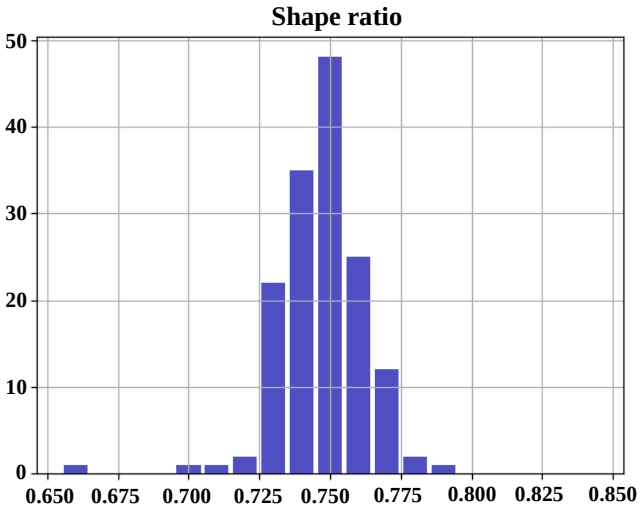

(d) Frequency distribution of stress shape factor R during the static loading stage

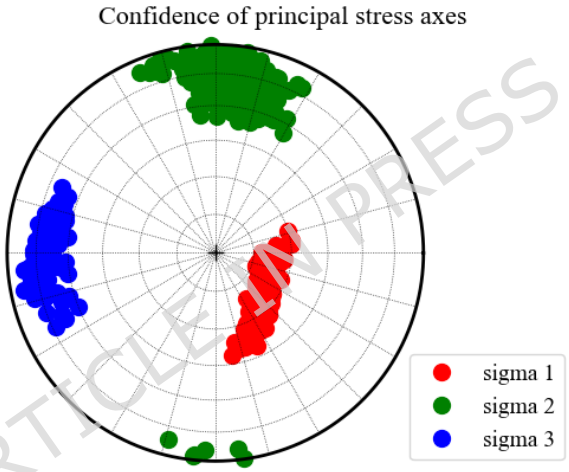

(e) Stress field direction during the secondary loading stage (confidence level 95%)

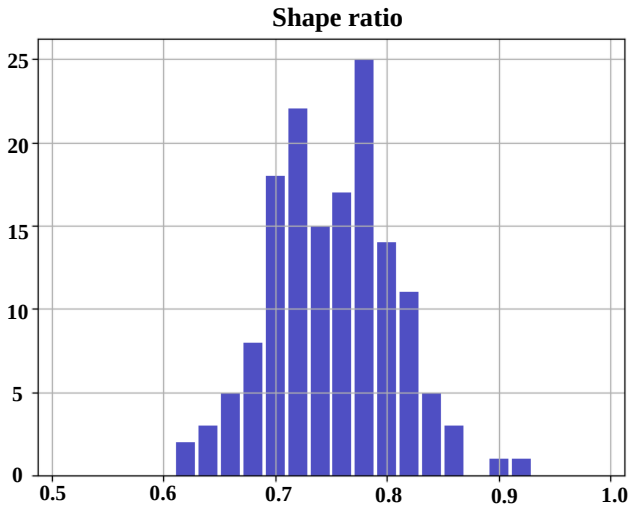

(f) Frequency distribution of stress shape factor R in the secondary loading stage

Figure 6. Inversion results of the local stress field of the coal body under drilling and pressure relief

Table 3 Main stress axis parameters in the initial loading stage

Stress axis	Azimuth/ (°)	Plunge/ (°)	R
σ_1	61.5	8.4	
σ_2	287.7	78.0	0.91
σ_3	152.8	8.6	

Table 4 Parameters of the principal stress axis during the static loading stage

Stress axis	Azimuth/ (°)	Plunge/ (°)	R
σ_1	324.2	10.7	
σ_2	54.9	4.0	0.75
σ_3	164.9	78.5	

Table 5 Main stress axis parameters in the secondary loading stage

Stress axis	Azimuth/ (°)	Plunge/ (°)	R
σ_1	140.6	62.1	
σ_2	8.9	19.4	0.78
σ_3	271.8	19.2	

During the initial loading phase, the stress field displays a typical three-dimensional heterogeneous state. The inversion results reveal that the azimuth of the maximum principal stress σ_1 is 61.5°, the dip angle is 8.4°, and the stress shape factor R reaches 0.91, indicating a shear-dominated oblique stress field within the coal body. The intermediate principal stress axis σ_2 (287.7°, 78.0°) is nearly vertical, forming an angle of approximately 226.2° with σ_1 and establishing an orthogonal stress system. The minimum principal stress σ_3 has an azimuth of 152.8° and a dip angle of 8.6°, and, along with σ_1, forms the dominant tensile-shear composite direction for initiating and propagating microfractures. This phase predominantly corresponds to the elastic deformation stage,

during which microcracks initiate within regions of stress concentration and propagate along the σ_1–σ_3 plane. The overall fracture mechanism is chiefly shear-based with minor tensile characteristics. In the static constant load phase, the stress field of the coal body becomes increasingly isotropic, with the stress state characterised by weak shear and strong compression.

The principal stress axis σ_1 shifts to an azimuth of 324.2° and a dip angle of 10.7°, whereas the shape factor R decreases to 0.75. This indicates that the coal body is nearing a hydrostatic pressure state, and the internal stress level is significantly reduced. The principal stress axes σ_2 and σ_3 correspond to azimuths of 54.9° and 164.9°, and dip angles of 4.0° and 78.5°, respectively. These three axes are nearly orthogonal, forming a typical homogeneous oblique stress field pattern. At this stage, the stabilisation of external disturbances and the complete release of prior damage lead to a reduced propagation rate of microfractures. Consequently, the stress field exhibits a low-energy shear mechanism dominated by compression. In the secondary loading stage, the stress field undergoes substantial restructuring, highlighting the diminishing influence of previously accumulated damage on coal strength and the asymmetry of stress concentration in later stages. The maximum principal stress σ_1 shifts to an azimuth of 140.6° and a dip angle of 62.1°, with the shape factor R increasing to 0.78, approaching the critical shear failure threshold. The shear forces intensify during this stage, governing the swift propagation of microcracks along the inclined fracture plane. The minimum principal stress σ_3 exhibits an azimuth of 271.8° and a dip angle of 19.2°, indicating near-horizontal tensile stress components that cause local lateral expansion. The overall fracture mechanism shifts from a shear-compression mode to a shear-tension composite mechanism, displaying notable asymmetry and local instability.

A 3D visualisation of the stress field was not included because the spatial resolution of the inversion results is constrained by the limited number of AE source locations and their planar distribution around the specimen. Under these conditions, a 3D representation would not provide additional meaningful structural information beyond the 2D results presented here and may instead create misleading artefacts. Therefore, the stress field is illustrated in two dimensions to maintain interpretational reliability.

Generally, the stress field within coal bodies demonstrates distinct stage-dependent evolutionary patterns under multi-stage loading. In the initial loading stage, a fundamental stress framework dominated by shear concentration is established. During the static loading stage, stress homogenisation and energy dissipation occur through stress relaxation. In the secondary loading stage, stress redistribution results from the cumulative effects of structural damage, ultimately triggering an asymmetric fracture mode governed by inclined shear and tensile coupling.

5 Discussion

This study systematically reveals the damage evolution of drilled coal bodies from elastic energy storage to critical penetration through multi-stage loading-unloading experiments. Macroscopic failure characteristic analysis indicates that the spatiotemporal distribution of AE events shows significant stage-dependent differences in mechanical response. Microscopic fracture mechanism analysis, based on moment tensor inversion and stress field inversion, uncovers the mechanical essence of damage in drilled coal under unloading conditions, validating the coupling relationship between macroscopic observations and microscopic mechanisms.

5.1 Theory of Drilling Hole Pressure Relief and Coal Mass Deformation and Failure

5.1.1 Mechanical mechanism of fracture propagation in drilled coal

An elastic mechanical model for the drilled hole unloading coal body is developed based on the initial elastic deformation state of the coal body prior to plastic failure during unloading, as shown in Figure 7. In this model, the initial horizontal stress component in the far field around the drilled hole unloading coal body is $\lambda\sigma$, where λ denotes the lateral pressure coefficient, and the initial vertical stress component is σ.

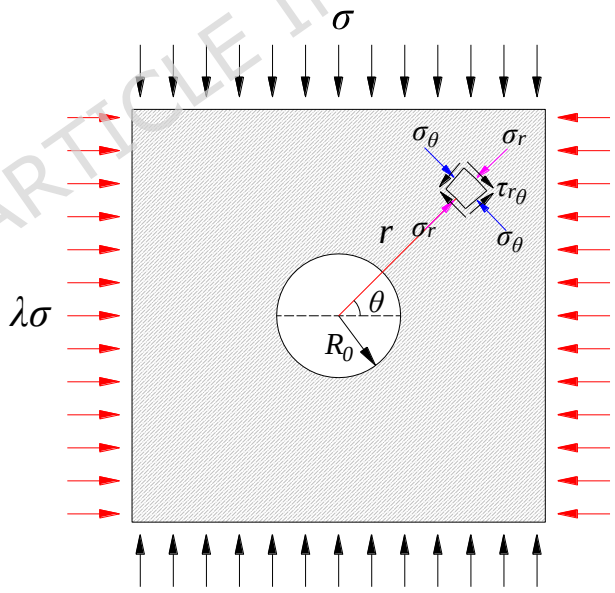

Figure 7 Mechanical model of coal pressure relief during drilling

The stress components of the drilled coal body under a non-uniform stress field were derived in the polar coordinate system [60]:

$$\begin{cases} \sigma_r = \frac{(\lambda+1)\sigma}{2}\left(1-\frac{R_0^2}{r^2}\right)+\frac{(\lambda-1)\sigma}{2}\left(1+\frac{3R_0^4}{r^4}-\frac{4R_0^2}{r^2}\right)\cos 2\theta \\ \sigma_\theta = \frac{(\lambda+1)\sigma}{2}\left(1+\frac{R_0^2}{r^2}\right)-\frac{(\lambda-1)\sigma}{2}\left(1+\frac{3R_0^4}{r^4}\right)\cos 2\theta \\ \tau_{r\theta} = -\frac{(\lambda-1)\sigma}{2}\left(1-\frac{3R_0^4}{r^4}+\frac{2R_0^2}{r^2}\right)\sin 2\theta \end{cases} \tag{13}$$

In the formula, $\boldsymbol{R}_0$ denotes the drill hole radius, $\boldsymbol{r}$ represents the distance from the coal stress calculation unit to the drill hole centre, and $\boldsymbol{\theta}$ denotes the angle between the line connecting the coal stress calculation unit to the drill hole centre and the horizontal stress direction.

Utilising the elastic mechanics model of the unloaded coal surrounding the drilled hole, the stress distribution under various lateral pressure coefficients was calculated and analysed, with the vertical stress on the unloaded coal set at 10 MPa and the drill hole radius fixed at 75 mm. Figure 8 illustrates the principal stress distribution of the unloaded coal under different lateral pressure coefficients.

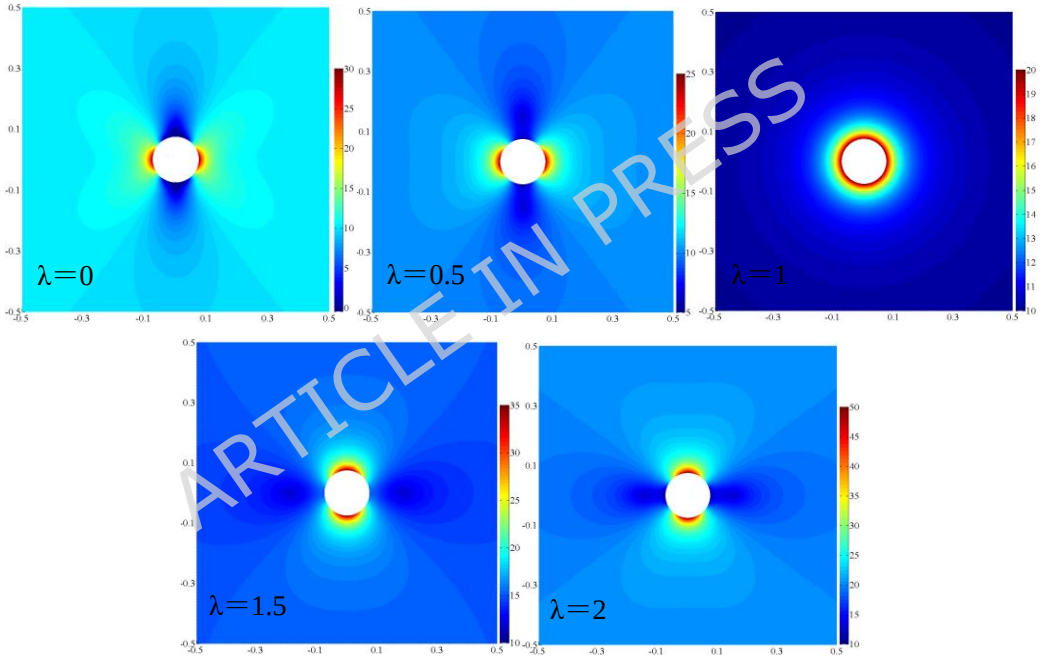

(a) Distribution of maximum principal stress in coal body

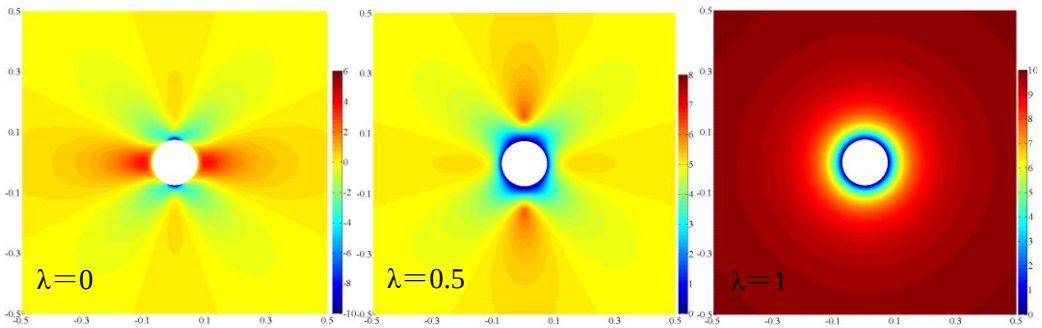

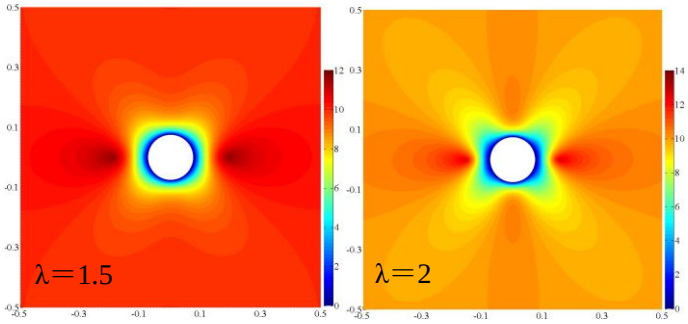

(b) Minimum principal stress distribution of coal body

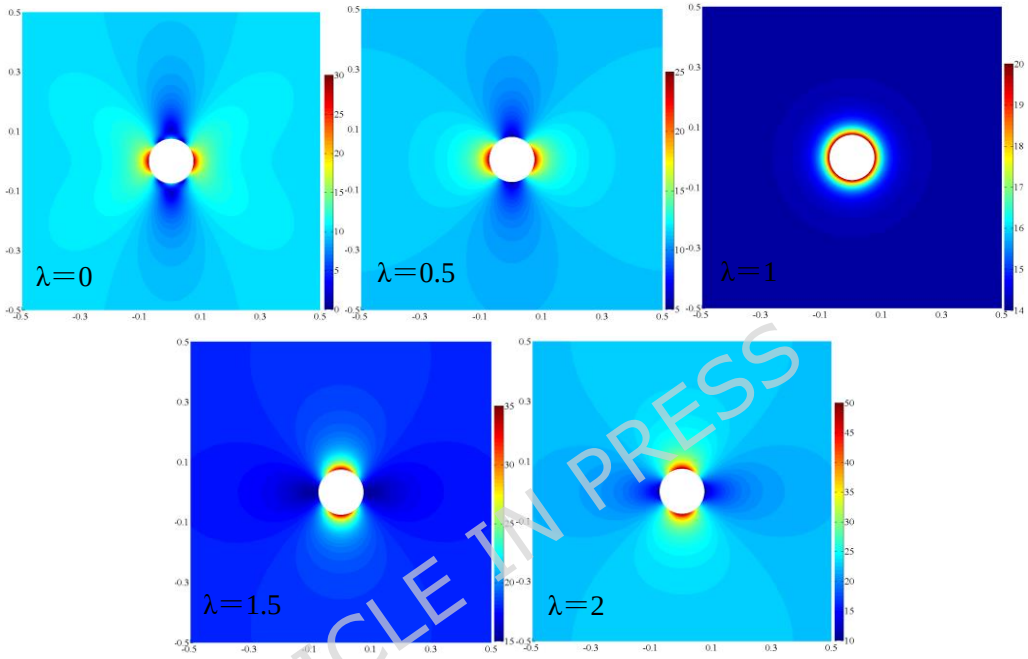

(c) Coal body combined stress distribution

Figure 8 Main stress distribution in coal body

Based on the stress distribution characteristics observed during drilling, it is concluded that, aside from unidirectional stress, no significant tensile stress concentration occurs around the drill hole. When the lateral pressure coefficient is below 1, the maximum principal and resultant stresses significantly concentrate at the horizontal ends of the drill hole, indicating that coal fractures initiate and propagate there. Conversely, when the lateral pressure coefficient exceeds 1, substantial stress concentrations develop at the vertical ends of the drill hole, suggesting that fractures commence and extend vertically. When the lateral pressure coefficient equals 1, high-stress concentration zones are evenly distributed around the drill hole, implying uniform fracture propagation.

Analysing stress level characteristics reveals a strong correlation between the stress distribution of the coal body under drilling and unloading conditions and the lateral pressure coefficient. Specifically, as the lateral pressure coefficient increases, leading to heightened horizontal stress, stress concentrations within the coal body exhibit a clear upward trend. Figure 9 depicts the

relationship between the stress concentration coefficient of the coal body under unloading conditions and various lateral pressure coefficients. Starting with a lateral pressure coefficient of 1, the stress concentration coefficient exhibits a pronounced logarithmic increase as the lateral pressure coefficient rises, achieving a correlation coefficient exceeding 0.99. This indicates that, under constant vertical stress conditions, an increase in vertical stress leads to a logarithmic escalation in stress concentration within the unloaded coal body.

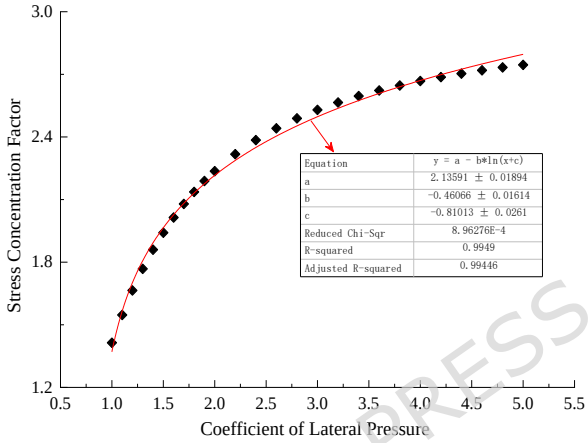

Figure 9: Fitting relationship between the stress concentration coefficient of the drilled and unloaded coal body and the lateral pressure coefficient

5.1.2 Model of weakening of coal body strength in drill holes

Following drilling and pressure relief, the stress state of the coal body rapidly adjusts, and plastic deformation progressively propagates from the drill hole outward, ultimately forming a fractured zone, plastic zone, and elastic zone arranged sequentially from the drill hole to the surrounding area. Considering the distribution characteristics of the coal body across various regions following pressure relief, an elastic-plastic mechanical model for drilling and pressure relief of the coal body was developed, as illustrated in Figure 10. Utilising the principal stress-defined strength criteria of the coal rock mass, the yield conditions for the unloaded coal mass around the drilled hole under planar strain conditions were established [61]:

$$f = \sigma_\theta - K\sigma_r - M = 0 \tag{14}$$

where $K = \frac{1+\sin\varphi}{1-\sin\varphi}$; $M = \frac{2C\cdot\cos\varphi}{1-\sin\varphi}$; φ represents the internal friction angle of the coal (°); C represents the cohesive strength of the coal, MPa.

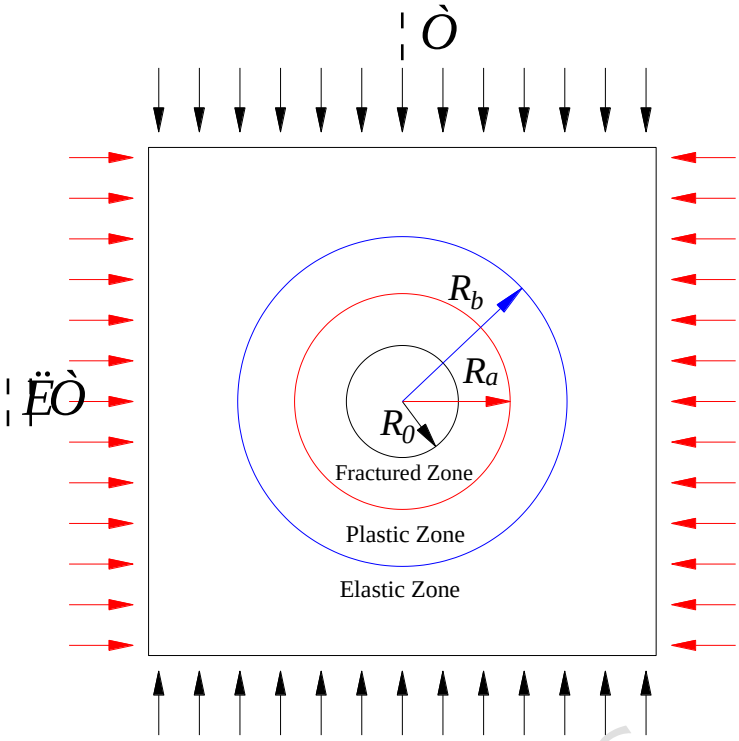

Figure 10: Drilling hole pressure relief coal body elastic-plastic mechanical model

Based on the force equilibrium equation under the plane strain assumption, the non-uniform stress field acting on the drilled coal body was decomposed into a uniform stress field and a stress field characterized by tension on one side and compression on the other. Applying the boundary conditions at the elastic-plastic transition point, the radial stress expression for the elastic-plastic transition of the drilled and unloaded coal body was derived as follows:

$$\sigma_r^{es}=\frac{(1+\lambda)\sigma+2(1-\lambda)\sigma\cos 2\theta-M}{K+1} \tag{15}$$

Subsequently, a model describing the reduction of coal strength under borehole pressure relief was developed. It was determined that the extent of the plastic zone distribution in coal during borehole pressure relief is influenced by factors including in-situ stress distribution (stress level and lateral stress coefficient), friction angle φ, cohesion C, and borehole diameter. The distribution ranges of the plastic zone under various borehole pressure relief conditions are illustrated in Figure 11.

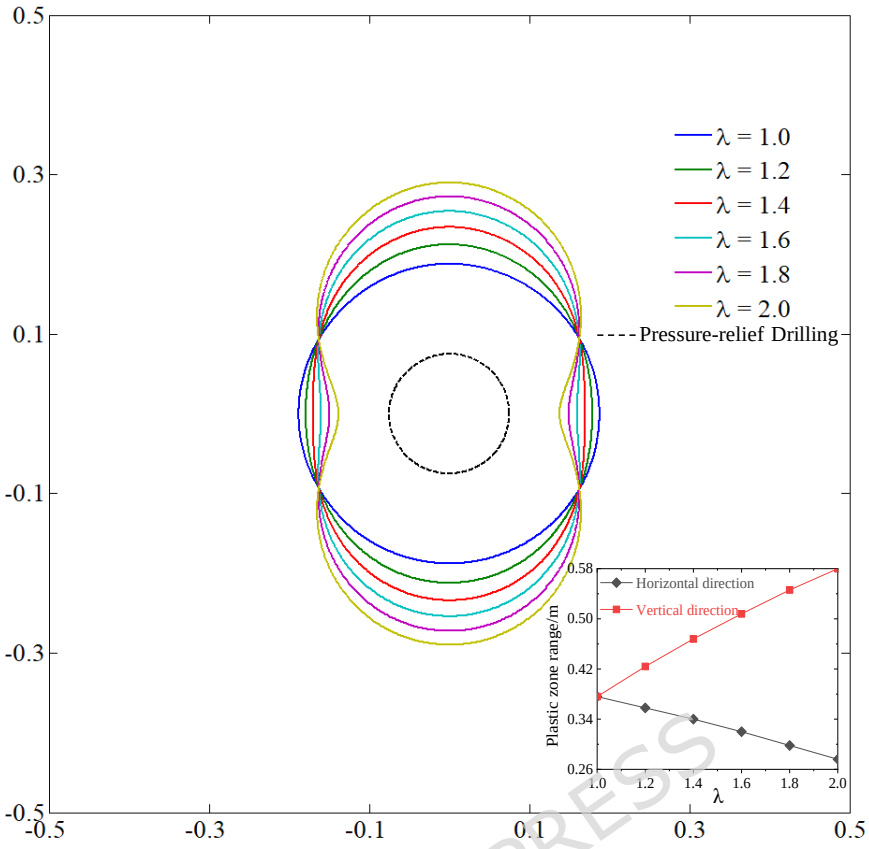

(a) Distribution range of plastic zones in coal bodies under different side pressure coefficients during drilling

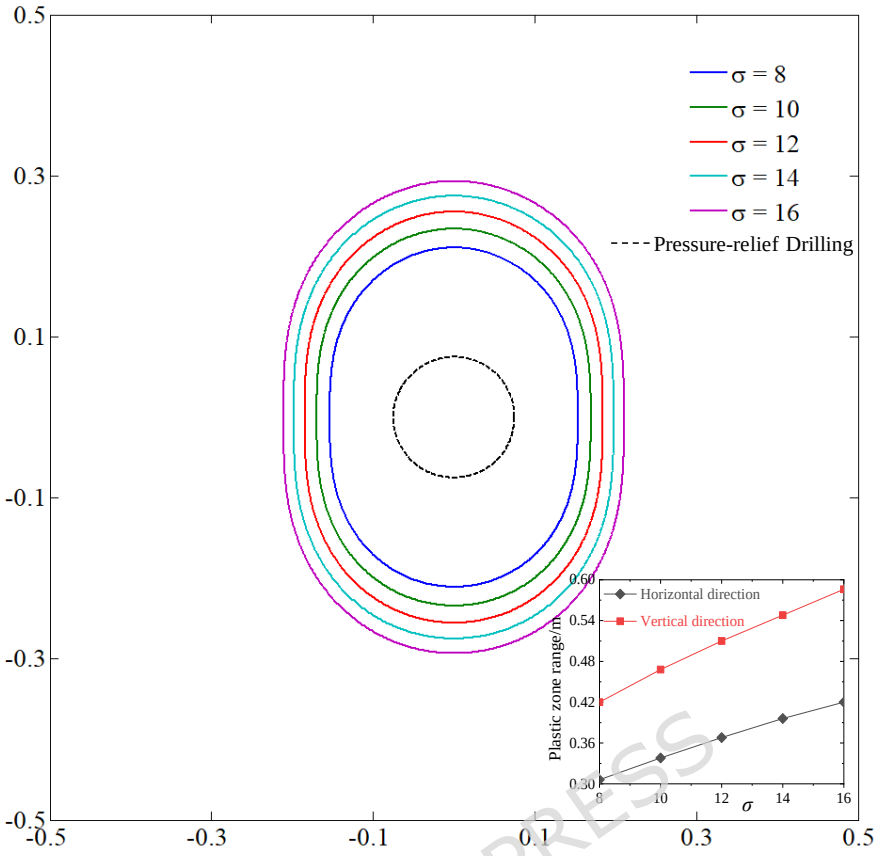

(b) Distribution range of plastic zones in coal bodies under different stress levels during drilling and pressure relief

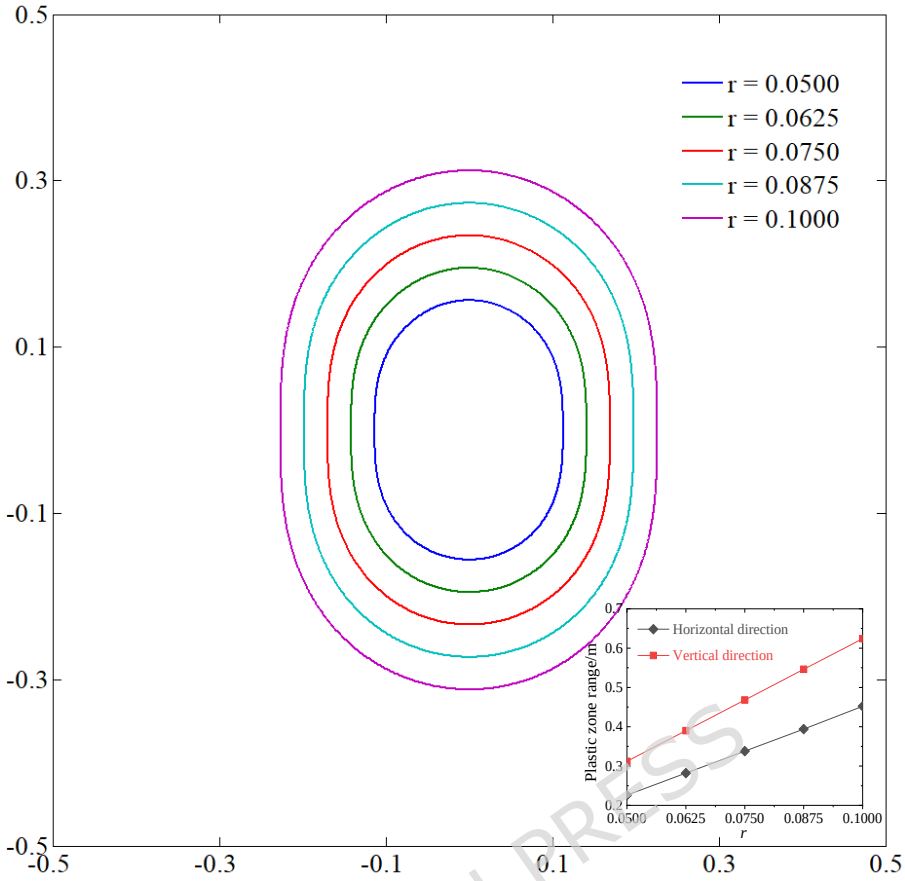

(c) Distribution range of plastic zones in coal bodies under drilling pressure relief at different borehole diameters

Figure 11 Distribution range of plastic zones in coal bodies under different conditions during drilling and pressure relief

(1) Influence of Lateral Pressure Coefficient λ on the Reduction of Strength in the Unloaded Coal Body

The unloaded coal body was subjected to a vertical stress of 10 MPa, a drill hole radius of 75 mm, an internal friction angle φ of 30°, and a residual cohesion C_b of 0.5 MPa. The extent of the plastic zone was evaluated under varying lateral pressure coefficients (λ = 1.0, 1.2, 1.4, 1.6, 1.8, and 2.0), as illustrated in Figure 12(a). Under a uniform stress field (λ = 1), the plastic zone surrounding the drilled-hole unloaded coal body is symmetrically distributed in a circular pattern. For lateral pressure coefficients between 1.2 and 1.4, the plastic zone predominantly assumes an elliptical shape. When the lateral pressure coefficient increases to 1.6, a “depression” formation emerges in the horizontal direction of the plastic zone. As the lateral pressure coefficient continues to rise, the plastic zone expands vertically while contracting horizontally.

(2) Influence of Stress Level on the Diminished Strength of the Unloaded Coal Body

Using a lateral pressure coefficient of 1.4, a borehole radius of 75 mm, an internal friction angle

(φ) of 30°, and a residual cohesion (C_b) of 0.5 MPa, the plastic zone extent was examined across various stress levels (σ = 8 MPa, 10 MPa, 12 MPa, 14 MPa, and 16 MPa). As illustrated in Figure 12(b), the plastic zones surrounding the drilled-hole unloaded coal body display an elliptical distribution at different stress levels. With increasing stress, the plastic zone expands in both vertical and horizontal directions, with a more pronounced growth vertically compared to horizontally.

(3) Influence of Drill Hole Diameter on the Diminished Strength of the Unloaded Coal Body

At a vertical stress of 10 MPa, a lateral pressure coefficient of 1.4, an internal friction angle (φ) of 30°, and a residual cohesion (C_b) of 0.5 MPa, the plastic zone extent was evaluated for varying borehole diameters (r = 50 mm, 62.5 mm, 75 mm, 87.5 mm, and 100 mm), as depicted in Figure 12(c). Under different borehole diameters, the plastic zone surrounding the drilled-hole unloaded coal body similarly exhibits an elliptical distribution. As borehole diameter increases, the plastic zone expands progressively in both vertical and horizontal directions, with vertical expansion occurring more rapidly than horizontal.

The morphology of the plastic zone within the coal body during drilling and pressure relief is primarily influenced by the lateral pressure coefficient applied to the coal. The size of the plastic zone is determined by the lateral pressure coefficient, stress level, and borehole diameter. Specifically, the lateral pressure coefficient dictates the shape of the weakened coal body under pressure relief, while the stress level and borehole diameter affect only the extent of the weakened zone.

5.2 Multiparameter comparison analysis of AE events in drilled coal bodies with different borehole diameters

Figure 12 presents a multiparameter comparison of AE events in drilled coal bodies across borehole diameters of 8 mm, 10 mm, and 12 mm. It should be explicitly noted that due to the discrete nature of acoustic emission events and their high sensitivity to microscopic local coal heterogeneity, directly averaging parameters (such as peak stress, total energy, and maximum ring counts) across multiple repeated samples can unscientifically smear out the true, abrupt physical bursting characteristics. Therefore, the curves and data points presented in Figure 12 are derived from a single typical and representative specimen for each condition. This comparison highlights the regulatory influence of borehole diameter on the robust damage accumulation patterns and energy release characteristics.

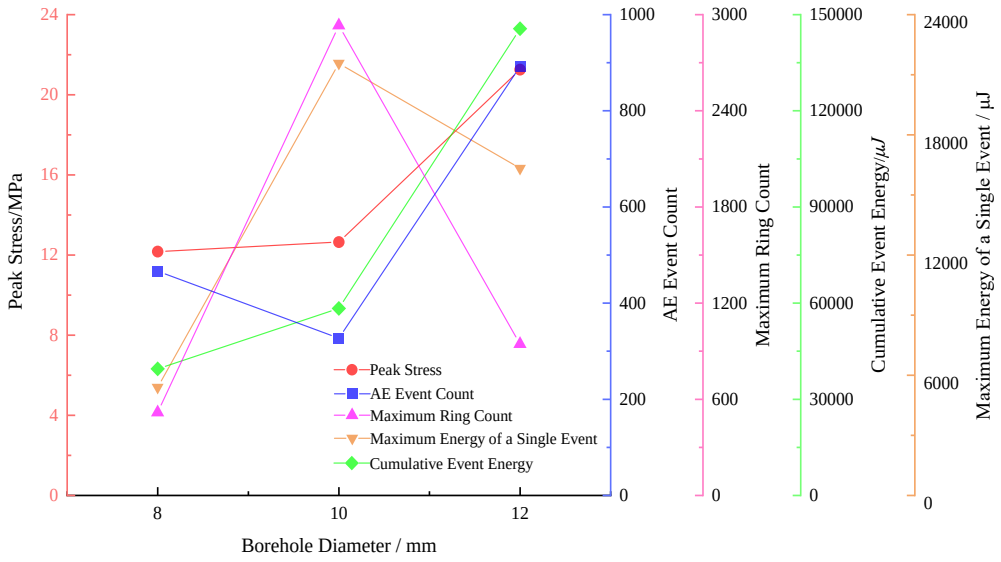

Figure 12 Multiparameter comparison of AE events in coal bodies from boreholes with different hole diameters. (Note: The data points and parameter comparisons presented in this figure represent the experimental results from a single typical experiment for each borehole diameter condition.)

It should be explicitly noted that due to the discrete nature of acoustic emission events and their high sensitivity to microscopic local coal heterogeneity, directly averaging parameters across multiple repeated samples can unscientifically smear out the true, abrupt physical bursting characteristics. Therefore, the parameter comparisons presented in Figure 12 are derived from a single typical and representative specimen for each condition. The results indicate that the number of AE events exhibits a nonlinear relationship with borehole diameter: 466 events for an 8 mm diameter, decreasing to 327 events at 10 mm, and then sharply increasing to 892 events at 12 mm. The medium pore diameters effectively suppress microfracture activity, whereas large pore diameters facilitate more extensive crack propagation. Under 10 mm conditions, the maximum energy of a single event reached 21,570 μJ, which significantly exceeded the 5,387 μJ observed at 8 mm, indicating highly concentrated local fracture energy. Although the maximum energy diminished to 16,326 μJ at 12 mm, cumulative energy increased from 39,454 μJ at 8 mm to 145,619 μJ at 12 mm, suggesting that larger pore diameters promote the synergistic propagation of multiple cracks and enhance overall energy release capacity. The ringing count correlates with energy characteristics; the 10 mm specimen exhibited a peak ringing count of 2,932, substantially higher than the 517 observed in the 8 mm specimen, reflecting stronger crack interactions and more frequent microfracture activity. Conversely, the ringing count of the 12 mm specimen decreased to 944, indicating that as the main crack propagates, acoustic emission activity stabilises. Peak stress increases with borehole diameter, rising from 12.172 MPa at 8 mm to 21.256 MPa at 12 mm, indicating that larger borehole diameters induce more pronounced localised stress concentration and

consolidation effects.

Overall, varying hole diameters produce distinct fracture patterns: small diameters exhibit discrete microfractures, medium diameters demonstrate localised high-energy release, and large diameters lead to crack network penetration. This highlights the critical role of hole diameter in shaping coal damage pathways and energy release mechanisms.

5.3 Time–frequency characteristics analysis of AE event waveforms in drilled coal bodies

To investigate the energy release characteristics of drilled coal bodies under various fracture mechanisms, three representative AE events—shear, tensile, and compressive fractures—were selected during the static constant load stage. A time-frequency analysis method was employed for a multidimensional comparative study. The original AE waveforms for these events were processed using wavelet transform to generate joint representations in both time and frequency domains, providing dual perspectives: time-domain waveforms and time–frequency energy density distributions. The time-domain waveforms captured the temporal evolution of signal amplitude, while time–frequency plots utilised colour scales to illustrate the spatial distribution of energy density over time and frequency, as shown in Figure 13.

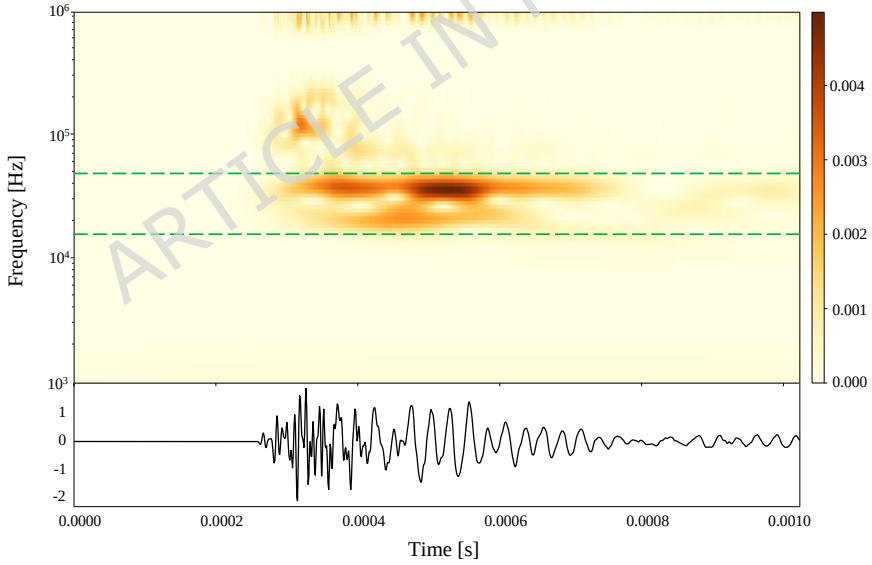

(a) Time–frequency distribution characteristics of tensile failure event waveforms (event 9)

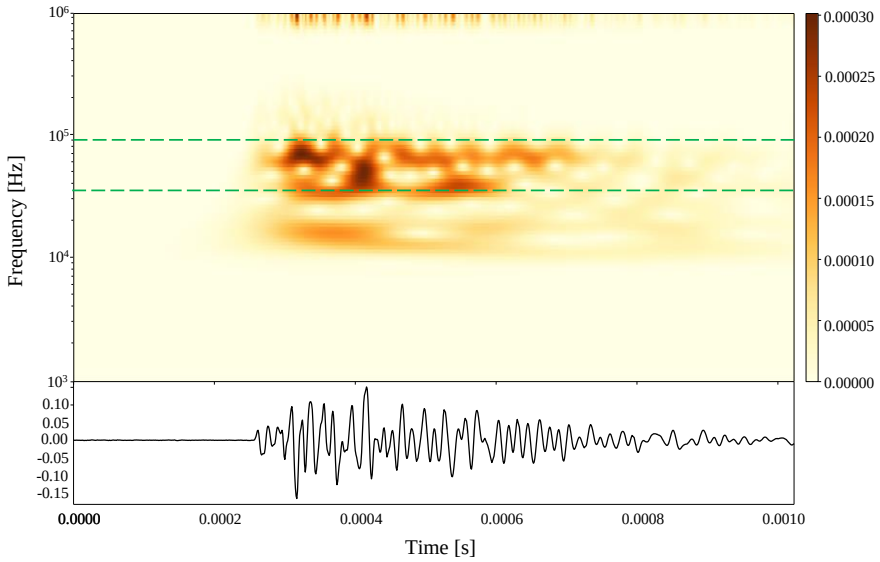

(b) Time–frequency distribution characteristics of shear failure event waveforms (event 10)

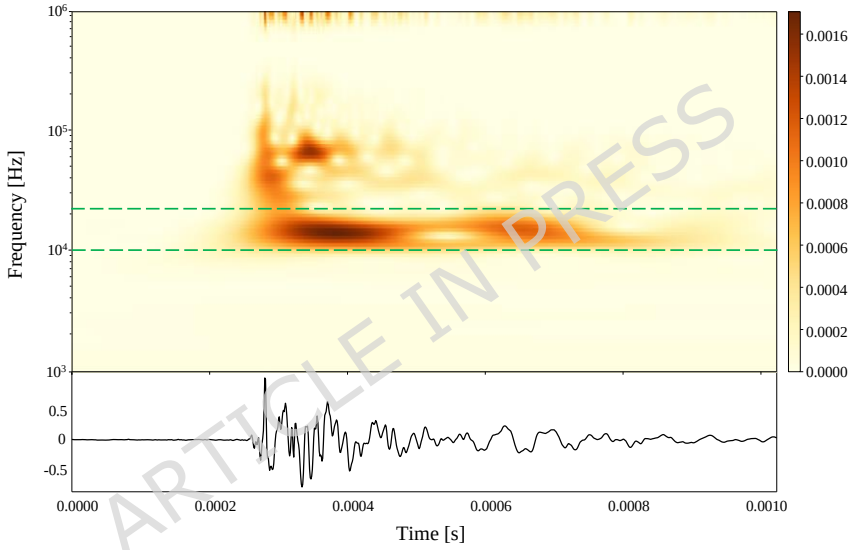

(c) Time–frequency distribution characteristics of compressed damage event waveforms (event 14)

Figure 13 Time-frequency distribution characteristics of waveforms for different fracture types

The present findings indicate that different rupture event types exhibit significant differences in main frequency range, waveform characteristics, and energy-time distribution. Specifically, shear fracture events have dominant frequencies concentrated between 80 and 90 kHz, with waveforms displaying abrupt pulse-like spikes followed by short-duration, high-frequency oscillations. The energy density rapidly accumulates within 0.25 ms and decays to near-background noise levels after 0.6 ms, exemplifying short-duration, high-frequency energy release characteristics. This behaviour is likely associated with the slip process along fracture surfaces. In contrast, tensile fracture events exhibit main frequencies in the 40–50 kHz range, with waveforms dominated by a single primary pulse followed by damped oscillations in the mid-frequency band. The time-frequency energy distribution exhibits a backward-expanding, fan-shaped pattern lasting approximately 0.25–0.8 ms,

highlighting the staged energy release behaviour associated with the gradual propagation of tensile cracks. Compression fracture events primarily occur within the low-frequency range of 10–20 kHz, characterised by low waveform amplitudes and prolonged durations, demonstrating multistage progressive changes. The time-frequency diagram displays a horizontal band-like distribution, indicating that low-frequency energy is emitted relatively steadily, likely linked to the pore closure process. A comparison of the three fracture modes reveals that shear fractures are identified by high frequency, short duration, and high amplitude characteristics; tensile fractures exhibit medium frequency, broad-band energy diffusion with moderate durations; and compressive fractures are marked by low frequency, sustained energy release, and significant time delays. Parameters such as frequency distribution range, energy accumulation, and decay rate can partially indicate fracture type and failure mechanisms.

6 Conclusions

This study investigates the fracture propagation behaviour of coal under drilling and unloading conditions. A multistage loading-unloading experimental system was developed, employing acoustic emission monitoring, moment tensor inversion, stress field inversion, and time-frequency spectrum analysis techniques to comprehensively examine the evolution mechanism of coal from microfracture to macro-instability. The main conclusions are as follows:

(1) Drilling-induced unloading alters the local stress field and coal microstructure. Although this process does not trigger immediate macroscopic failure, it leads to higher AE event frequency and energy release during secondary loading, reflecting the transition from dispersed microcracks to more oriented fracture development.

(2) Moment tensor inversion indicates a shift in fracture behaviour, initial and static loading stages are dominated by shear-related mechanisms, whereas secondary loading exhibits an increased contribution of tensile components, accompanied by normal and oblique-normal faulting.

(3) Stress field inversion reveals changes in principal stress orientations and stress shape factors across different stages. The stress state evolves from a shear-concentrated pattern to a near-isotropic distribution and subsequently to a reoriented shear-dominated configuration, with principal stresses rotating from a SW–NE to a SE–NW direction.

(4) Elastoplastic analysis shows that the plastic zone shape is mainly influenced by the lateral pressure coefficient, while its size depends on the stress level and borehole diameter.

(5) Time–frequency analysis distinguishes typical spectral signatures associated with different fracture behaviours: high-frequency bursts for shear-related events, mid-frequency signals for tensile-related activity, and low-frequency continuous emissions for compressional responses.

Under drilling and pressure relief conditions, the fracture propagation behaviour of coal

exhibits pronounced stress sensitivity and stage-dependent responses. Observations derived from acoustic emission analysis, moment tensor inversion, and stress field reconstruction collectively reveal characteristic patterns of microcrack activation and their subsequent evolution towards macroscale failure during loading. These findings provide insights into the coupled effects of unloading perturbations and external loading on crack propagation at the laboratory scale.

Acknowledgments

We gratefully wish to acknowledge the collaborative funding support from the National Natural Science Foundation of China (52104102).

Competing Interests Statement

The authors declare that there is no conflict of interests regarding the publication of this paper.

Data availability statement

The data that support the findings of this study are available from the corresponding author upon reasonable request.

Funding

This work was supported by the National Natural Science Foundation of China (Grant No. 52104102).

References

[1] Li T., Cai M.F., Cai M., 2007. A review of mining-induced seismicity in China. Int J Rock Mech Min Sci. 44, 1149-1171.

[2] Zhang C.G., Canbulat I., Hebblewhite B., Ward C.R., 2017. Assessing coal burst phenomena in mining and insights into directions for future research. Int J Coal Geol. 179, 28-44.

[3] Liu X.F., Xu G., Zhang C., Kong B., Qian J.F., Zhu D., Wei, M.Y., 2017. Time effect of water injection on the mechanical properties of coal and its application in rockburst prevention in mining. Energies. 10, 1783.

[4] Zhang, S.C., Li, Y.Y., Shen, B.T., Sun, X.Z., Gao, L.Q., 2019. Effective evaluation of pressure relief drilling for reducing rock bursts and its application in underground coal mines. Int J Rock Mech Min Sci. 114, 7-16.

[5] Yin, Y.C., Chen, B., Zhang, Y.B., He, S.D., Yao, C.R., Liu, C.C., 2024. Experimental study and evaluation on the weakening of bursting liability of coal with boreholes. Eng Fail Anal. 155, 107754.

[6] Fu, Y.K.,·Wu, Y.Z., Li·J,C., Zhou, P.H., Sun, Z.Y., He, J., 2024. Mechanical properties and energy evolutions of burst-prone coal samples with holes and fillings. Int J Coal Sci Techn. 11, 40.

[7] Zhang, L., Huang, P., Liu S.J., He, G., Li, B., Cao, Y.W., 2022. Relief Mechanism of Segmented Hole Reaming and Stress Distribution Characteristics of Drilling Holes in Deep Coal Mine. Processes. 10, 1566.

[8] Jiang, Z.H., Zhang, J.C., Yue, L.J., Li, D.H., 2025. Coordinated control of pressure relief and energy absorption support of deep mining roadway. Phys Fluids. 37, 047138.

[9] Yao, J.P., Yin, Y.C., Zhao, T.B., Ren, W.T., Qiu, Y., Guo W.Y., 2020. Segmented enlarged-diameter borehole destressing mechanism and its influence on anchorage support system. Energy Sci Eng. 8, 2831-2840.

[10] Du, S.Y., Zuo, Y.J., Chen, Q.G., Zheng, L.J., Rong, P., Liu, H., Jin, K.Y., Lin, J.Y., Chen, B., Xing, B., 2024. Study on the response characteristics of roadway borehole pressure relief surrounding rock under strike-slip high-stress distribution. Eng Fail Anal. 156, 107808.

[11] Hao, Z., Sun, G.Z., Wei, H.H., Liu, J.Y., Tian, M.L., Liu, S.Y., Xu, Y.K., 2021. Pressure-Relief Mechanism and Application of Large-Diameter Boreholes in Coal Seams with Rockburst Hazard. Geofluids. 2021, 5469999.

[12] Shi, Q.W., Mishra, B., Wang, S.W., Xu, G., 2021. In situ assessment of the effectiveness of an undisturbed single driving entry's relief borehole in coal burst-prone seam. Mining Metall Explor. 38, 2443-2452.

[13] Wu, H., Zhao, G.Y., Liang, W.Z., 2019. Investigation of cracking behavior and mechanism of sandstone specimens with a hole under compression. Int J Mech Sc. 163, 105084.

[14] He, Z.C., Gong, F.Q., Gao, M.Z., 2025. Experimental study on the mechanical behavior of high‐stress rocks during real‐time drilling. Int J Coal Sci Techn. 12, 37.

[15] Zhang, K., Chen, Y.L., Fan, W.C., Liu, X.H., Luan, H.B., Xie, J.B., 2020. Influence of intermittent artificial crack density on shear fracturing and fractal behavior of rock bridges: experimental and numerical studies. Rock Mech Rock Eng. 53, 553-568.

[16] Wang, Y.T., Zhou, X.P., Shou, Y.D., 2017. The modeling of crack propagation and coalescence in rocks under uniaxial compression using the novel conjugated bond-based peridynamics. Int J Mech Sci. 128-129, 614-643.

[17] Zhao, Y.S., Gao, Y.T., Wu, S.C., 2020. Influence of different concealment conditions of parallel double flaws on mechanical properties and failure characteristics of brittle rock under uniaxial compression. Theor Appl Fract Mec. 109, 102751.

[18] Wang, Y.X., Zhang, H., Lin, H., Zhao, Y.L., Liu, Y., 2020. Fracture behaviour of central-flawed rock plate under uniaxial compression. Theor Appl Fract Mec. 106, 102503.

[19] Xu, W.J., Khan, K.U.J., 2025. Multi-scale mechanical behaviors of rock mass based on synthetic rock mass. B Eng Geol Environ. 84, 130.

[20] Shen, B.T., Stephansson, O., Einstein, H.H., Ghahreman, B., 1995. Coalescence of fractures under shear stresses

in experiments. J Geophys Res Solid Earth. 100, 5975-5990.

[21] Bobet, A., Einstein, H.H., 1998. Fracture coalescence in rock-type materials under uniaxial and biaxial compression. Int J Rock Mech Min Sci. 35, 863-888.

[22] Guo, T.F., Zhang, Q., Liu, K.W., Chang, X., Zou, L.S., 2024. Co-effects of parallel flaws and interface characteristics on the fracture behavior of rock-concrete composite specimens. J Build Eng. 97, 110920.

[23] Shang, J., West, L.J., Hencher, S.R., Zhao, Z., 2018. Tensile strength of large-scale incipient rock joints: a laboratory investigation. Acta Geotech. 13, 869-886.

[24] Kutter, H.K., Fairhurst, C., 1971. On the fracture process in blasting. Int J Rock Mech Min Sci. 8, 181-202.

[25] Bobet, A., 2000. The initiation of secondary cracks in compression. Eng Fract Mech. 66, 187-219.

[26] Rossmanith, H.P., Knasmillner, R.E., Daehnke, A., Mishnaevsky, Jr.L., 1996. Wave propagation, damage evolution, and dynamic fracture extension. Part II. Blasting. Mater Sci, 32, 403-410.

[27] Yang, R.S., Ding, C.X., Li, Y.L., Yang, L.Y., Zhao, Y., 2019. Crack propagation behavior in slit charge blasting under high static stress conditions. Int J Rock Mech Min Sci. 119, 117-123.

[28] Wang, K., Zhang, X., Du, F., Li, K.N., Sun, J.Z., Wang, Y.Q., 2023. Numerical study on damage response and failure mechanism of gas-containing coal-rock combination under confining pressure effect. Fuel. 349, 128683.

[29] Liu, Y., Lu, C.P., Zhang, X.F., Guo, Y., Song, C.H., Wang, C., 2022. Failure and instability characteristics of coal-rock parting-coal structures with rough discontinuities. Rock Mech Rock Eng. 55, 7063-7080.

[30] Liu, S., Liu, H.D., Liu, H.N., Xia, Z.G., Zhao, Y.W., Zhai, J.Y., 2022. Numerical simulation of mesomechanical properties of limestone containing dissolved hole and persistent joint. Theor Appl Fract Mec. 122, 103572.

[31] Chen, M., Zhang, Y.L., Zang, C.W., Zhang, G.C., Li, Q., Jiang, B.Z., 2023. Experimental Investigation on Pressure Relief Mechanism of Specimens with Prefabricated Reaming Boreholes. Rock Mech Rock Eng. 56, 2949-2966.

[32] Chen, Y., Li, P.F., Xu, C.B., Chen, M., Yang, J.Y., 2024. Failure characteristics and pressure relief effectiveness of non-persistent jointed rock mass with holes. Theor Appl Fract Mec. 134, 104733.

[33] Liu, D.Q., Zhang, Z.Q., Yang, J.S., Sun, Q.F., Liu, Z.X., Sun, J., 2025. Effect of Borehole Pressure Relief on Rockburst: Insights from Borehole Cooperative Deformation Mechanism. Rock Mech Rock Eng. 58, 2295-2317.

[34] Zhang, Y.J., Chen, Y.X., Zhang, S., Feng, G.R., Wang, Y.G., Li, S.L., Wang, Q., Wang, B., Zhao, L., 2025. Study on the influence of drilling parameters on the mechanical properties and pressure relief effect of coal rock. Processes. 13, 993.

[35] Jing, G., Zhao, Y.X., Wang, H., Montanari, P.M., Lacidogna, G., 2024. Study of Coal and Magnetite Collapse Process and Precursor Based on Acoustic Emission Flicker Noise Spectroscopy. Rock Mech Rock Eng. 57, 8545-8562.

[36] Di, Y.Y., Wang, E.Y., Li, Z.H., Liu, X.F., Huang, T., Yao, J.J., 2024. Predicting microseismic, acoustic emission and electromagnetic radiation data using neural networks. J Rock Mech Geotech. 16, 616-629.

[37] Feng, J.Q., Li, B.L., Wang, E.Y., Liu, X.F., Li, N., Cao, X., Zhang, M., 2025. Intelligent recognition of electromagnetic radiation precursory signals of rock fracture based on random forest-adaptive boosting. Phys Fluids. 37, 046609.

[38] Liu, X.Y., Chai, Z.Y., Shen, Y.X., Xiao, C., Xin, Z.P., Li, T.Y., Sun, H.C., Liu, X.Y., Yan, K., Duan, B.Y., 2024. Evolution of deformation failure and energy of siltite and significant shear fracture structure under cyclic loading. Rock Mech Rock Eng. 57, 7835-7860.

[39] Liu, Z.L., Xie, S.L., Yin, Y.J., Su, T., 2025. Fractal characterization and pore evolution in coal under tri-axial cyclic loading-unloading: insights from low-field NMR imaging and analysis. Fractal Fract. 9, 93.

[40] Lockner, D., 1993. The role of acoustic emission in the study of rock fracture. Int J Rock Mech Min. 30, 883-899.

[41] Shkuratnik, V.L., Filimonov, Y.L., Kuchurin, S.V., 2005. Regularities of acoustic emission in coal samples under triaxial compression. J Min Sci. 41, 44-52.

[42] Moradian, Z., Einstein, H.H., Ballivy, G., 2016. Detection of cracking levels in brittle rocks by parametric analysis of the acoustic emission signals. Rock Mech Rock Eng. 49, 785-800.

[43] Song, M.Y., Hu, Q.T., Liu, H.H., Li, Q.G., Zhang, Y.B., Hu, Z.F., Liu, J.C., Deng, Y,Z., Zheng, X.W., Wang, M.J., 2023. Characterization and correlation of rock fracture-induced electrical resistance and acoustic emission. Rock Mech Rock Eng. 56, 6437-6457.

[44] Li, Q.G., Qian, Y.A., Hu, Q.T., Jiang, Z.Z., Xu, Y.C., Shang, X.Y., Ling, F.P., Liu, R.H., Li, W.X., 2022. Acoustic Emission Response Mechanism of Hydraulic Fracturing in Different Coal and Rock: A Laboratory Study. 55, 4657-4672.

[45] Zhang, W., Ma, Q., Liu, X.L., Wang, E.Z., Xie, W.Q., Song, D.Q., 2024. Study on crack propagation mechanism and acoustic-thermal sensitivity analysis of pre-cracked weakly cemented rock. Theor Appl Fract Mec. 133, 104619.

[46] Qian, R.P., Feng, G.R., Guo, J., Wang, P.F., Wen, X.Z., Song, C., 2022. Experimental investigation of mechanical characteristics and cracking behaviors of coal specimens with various fissure angles and water-

bearing states. Theor Appl Fract Mec. 120, 103406.

[47] Dai, J.J., Liu, J.F., Zhou, L.L., He, X., 2023. Crack pattern recognition based on acoustic emission waveform features. Rock Mech Rock Eng. 56, 1063-1076.

[48] Lacidogna, G., Piana, G., Carpinteri, A., 2019. Damage monitoring of three-point bending concrete specimens by acoustic emission and resonant frequency analysis. Eng Fract Mech. 210, 203-211.

[49] Lan, M., Tang, Y., Ma, J., Liu, Z.X., 2023. Cooperative acoustic emission locating with velocity tomography in true triaxial experiment. Eng Fract Mech. 292, 109633.

[50] Zhu, G.A., Dou, L.M., Wang, C.B., Ding, Z.W., Feng, Z.J., Xue, F., 2019. Experimental study of rock burst in coal samples under overstress and true-triaxial unloading through passive velocity tomography. Safety Sci. 117, 388-403.

[51] Kong, Y., Li, M., Chen, W.M., Liu, N., Kang, B.Q., 2021. Moment-tensor inversion and decomposition for cracks in thin plates. Chinese J Aeronaut. 34, 352-359.

[52] Liu, J.P., Li, Y.H., Xu, S.D., Xu, S., Jin, C.Y., Liu, Z.S., 2015. Moment tensor analysis of acoustic emission for cracking mechanisms in rock with a pre-cut circular hole under uniaxial compression. Eng Fract Mech. 135, 206-218.

[53] Davi, R., Vavrycuk, V., Charalampidou, E.M., Kwiatek, G., 2013. Network sensor calibration for retrieving accurate moment tensors of acoustic emissions. Int J Rock Mech Min Sci. 62, 59-67.

[54] Sedlak P, Hirose Y, Khan S A, et al. New automatic localization technique of acoustic emission signals in thin metal plates[J]. Ultrasonics, 2009, 49(2): 254-262

[55] Li X, Dong L. An efficient closed-form solution for acoustic emission source location in three-dimensional structures[J]. AIP advances, 2014, 4(2).

[56] White J E. Underground sound: Application of seismic waves[J]. 2000.

[57] Feignier B, Young R P. Moment tensor inversion of induced microseisnmic events: Evidence of non-shear failures in the− 4< M<− 2 moment magnitude range[J]. Geophysical Research Letters, 1992, 19(14): 1503-1506.

[58] Stockwell R G, Mansinha L, Lowe R P. Localization of the complex spectrum: the S transform[J]. IEEE transactions on signal processing, 2002, 44(4): 998-1001.

[59] Vavryčuk, V. (2014). Iterative joint inversion for stress and fault orientations from focal mechanisms. Geophysical Journal International, 199(1), 69-77.

[60] Xu Z. Elastic Mechanics [M]. Beijing: Higher Education Press, 2006.

[61] Deng C, Zheng Y, Zhu J. Formula of intermediate principal stress at yield of Mohr-Coulomb material under plane strain condition[J]. Rock and Soil Mechanics, 2008, 29(2): 5.